Nano Research

ISSN 1998-0124 CN 11-5974/O4
https://doi.org/10.26599/NR.2026.94909258

Research Article

Geometry-driven confinement and iodine evolution in robust metal–organic frameworks for adsorptive iodine storage

Wenqi Wang[1], Weixiang Zuo[1], Zhe Wang[1], Wentao Jiang[1], Hao Chen[1], Xinyi Xu[1], Xu-Dong Wu[3], Mian Li[3], Yingbo Zhao[1], Zheng Yin[2](✉), Ming-Hua Zeng[2,3](✉), Yue-Biao Zhang[1](✉)

[1] Institute of Carbon Neutrality, School of Physical Science and Technology, Shanghai Key Laboratory of High-Resolution Electron Microscopy, and State Key Laboratory of Advanced Medical Materials and Devices, ShanghaiTech University, Shanghai 201210, China

[2] Key Laboratory for Chemistry and Molecular Engineering of Medicinal Resources (Ministry of Education of China), Guangxi Key Laboratory of Chemistry and Molecular Engineering of Medicinal Resources, School of Chemistry and Pharmaceutical Sciences, Guangxi Normal University, Guilin 541004, China

[3] College of Chemistry and Chemical Engineering, Key Laboratory for Preparation and Application of Ordered Structural Materials of Guangdong Province, Shantou University, Guangdong 515063, China

Nano Res., **Just Accepted Manuscript** • https://doi.org/10.26599/NR.2026.94909258
https://www.sciopen.com/journal/1998-0124 on Oct. 12, 2026

© The Authors(s)

Just Accepted

This is a "Just Accepted" manuscript, which has been examined by the peer-review process and has been accepted for publication. A "Just Accepted" manuscript is published online shortly after its acceptance,which is prior to technical editing and formatting and author proofing. Tsinghua University Press (TUP) provides "Just Accepted" as an optional and free service which allows authors to make their results available to the research community as soon as possible after acceptance. After a manuscript has been technically edited and formatted, and the page proofs have been corrected, it will be removed from the "Just Accepted" web site and published officially with volume and article number (e.g., *Nano Research*, **2025**, *18*, 94906990). Please note that technical editing may introduce minor changes to the manuscript text and/or graphics which may affect the content, and all legal disclaimers that apply to the journal pertain. In no event shall TUP be held responsible for errors or consequences arising from the use of any information contained in these "Just Accepted" manuscripts. To cite this anuscript please use its Digital Object Identifier (DOI®),which is identical for all formats of publication.

TABLE OF CONTENTS (TOC)

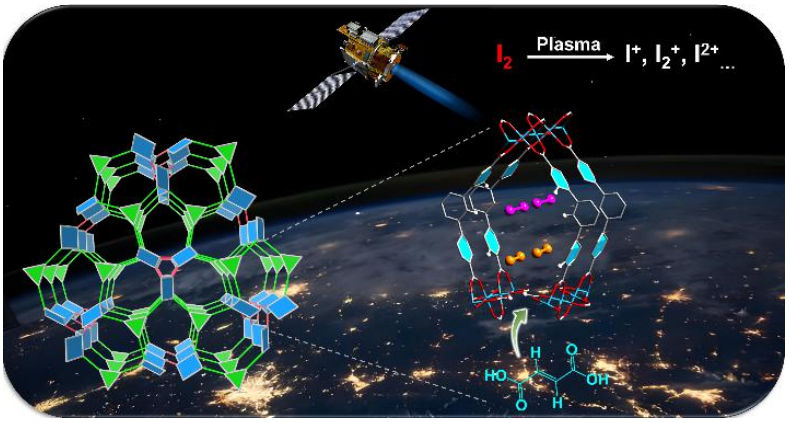

Geometry-driven confinement within 1D metal-organic framework channels yields ultrahigh iodine density; subsequent isoreticular retrofitting ensures robust, fully reversible high-capacity storage.

Just Accepted

Nano Research

Open Access

Research Article

Geometry-driven confinement and iodine evolution in robust metal–organic frameworks for adsorptive iodine storage

Wenqi Wang[1], Weixiang Zuo[1], Zhe Wang[1], Wentao Jiang[1], Hao Chen[1], Xinyi Xu[1], Xu-Dong Wu[3], Mian Li[3], Yingbo Zhao[1], Zheng Yin[2] ✉, Ming-Hua Zeng[2,3] ✉, and Yue-Biao Zhang[1] ✉

[1] *Institute of Carbon Neutrality, School of Physical Science and Technology, Shanghai Key Laboratory of High-Resolution Electron Microscopy, and State Key Laboratory of Advanced Medical Materials and Devices, ShanghaiTech University, Shanghai 201210, China*

[2] *Key Laboratory for Chemistry and Molecular Engineering of Medicinal Resources (Ministry of Education of China), Guangxi Key Laboratory of Chemistry and Molecular Engineering of Medicinal Resources, School of Chemistry and Pharmaceutical Sciences, Guangxi Normal University, Guilin 541004, China*

[3] *College of Chemistry and Chemical Engineering, Key Laboratory for Preparation and Application of Ordered Structural Materials of Guangdong Province, Shantou University, Guangdong 515063, China*

Received: 9 October 2206; **Accepted:** 12 October 2026

✉Address correspondence to Zheng Yin, yinzheng@mailbox.gxnu.edu.cn; Ming-Hua Zeng, zmh@mailbox.gxnu.edu.cn; Yue-Biao Zhang, zhangyb@shanghaitech.edu.cn

Cite this article: *Nano Research*, 2026, 19, 94909258 https://doi.org/10.26599/NR.2026.94909258

ABSTRACT: Efficient volatile iodine uptake and release is crucial for nuclear waste remediation and aerospace propulsion. However, current sorbents often face a trade-off between high capacity and facile regeneration, as strong host–guest interactions can hinder low-energy iodine release. Here, we report a reticular chemistry strategy combining geometry-driven confinement and structural retrofitting to address this challenge. In MOF-521, favorable geometric matching between one-dimensional rhombic channels and I_2 molecules promotes dense iodine confinement, achieving an intrapore packing density of 3.18 g cm^{-3} and utilizing approximately 65% of the available pore space. Comprehensive investigations integrating single-crystal X-ray diffraction (SCXRD), three-dimensional electron diffraction (3D ED), powder X-ray diffraction (PXRD), Raman and XPS spectroscopy, electrical conductivity measurements, and theoretical calculations reveal a dual-stage synergistic capture mechanism. Initial iodine incorporation involves speciation evolution and charge redistribution, followed by progressive geometry-confined physical filling and dense iodine organization. SCXRD further resolves ordered iodine assemblies with short I···I contacts, highlighting the role of spatial confinement in promoting dense packing. However, such confined packing also contributes to framework deformation during desorption. Replacing monodentate formate with ditopic fumarate yields MOF-521-Fum with a distinct **wwq** topology. This structural retrofit maintains a high intrapore packing density of 2.79 g cm^{-3}, raises the decomposition temperature by 200 °C, enables complete iodine desorption, and achieves 96% capacity retention after four cycles. These findings highlight geometry-driven confinement and targeted structural regulation as complementary strategies for balancing dense iodine storage and reversible release.

KEYWORDS: metal–organic frameworks; geometry-driven confinement; adsorptive iodine storage; structural retrofitting.

Just Accepted

1 Introduction

The adsorption and storage of volatile iodine are critical not only for the environmental remediation of radioactive isotopes (^{129}I and ^{131}I) during nuclear fuel reprocessing [1,2], but also for the emerging aerospace propulsion technology. Recently, iodine has been shown to be a highly efficient propellant for electric propulsion systems in miniaturized satellites (e.g., CubeSats), outperforming conventional xenon gas [3,4]. These demanding applications require ideal storage media to possess high volumetric packing density for maximum storage capacity, reversible desorption kinetics for facile release, and robust structural stability for extended cycling.

Metal–organic frameworks (MOFs) are crystalline porous materials with predictable network structures, tunable pore metrics, and chemically tailorable pore environments [5], making them promising platforms for iodine adsorption and for elucidating structure–property relationships [6-8]. Extensive research has elegantly demonstrated π-electronic charge transfer [9-11], chemisorption [12-14], confined polyiodide structures [15-18], and enhanced chemical stability to achieve improved iodine uptake. These advances have highlighted the importance of pore chemistry and spatial confinement in determining iodine adsorption behavior [19-21]. Despite these significant advances, simultaneously achieving high iodine loading density, reversible release, and long-term structural stability remains challenging. Increasing pore volume and enlarging channel dimensions can provide more accommodation space and improve the overall iodine uptake. However, excessive pore expansion reduces the interaction density between iodine

molecules and the pore surfaces, leading to inefficient molecular packing. Conversely, introducing strong chemical binding sites can effectively stabilize iodine species and enhance adsorption strength, but excessive host–guest interactions increase the energetic barrier for iodine release and compromise regeneration efficiency. Therefore, developing targeted iodine storage materials requires a design strategy that maximizes iodine packing while maintaining weak and reversible host-guest interactions.

To navigate this balance, we explore a strategy based on geometry-driven confinement and isoreticular fine-tuning to optimize physical adsorption. Considering the effective interaction range of molecular iodine (~5 Å) [22,23], recent investigations have established that pores with moderate diameters (6-8 Å) and tailored 1D channels provide an ideal confined space for the ordered assembly of iodine molecules, enabling efficient packing and high storage density [15]. Guided by this fundamental premise, we hypothesize that a pristine pore environment, geometrically tailored to these specific dimensions, can provide sufficient van der Waals potential overlap without relying on strong chemical interaction.

Herein, we develop an Al-based metal–organic framework, MOF-521, as a model platform to demonstrate a geometry-driven strategy for high density iodine storage. MOF-521 is constituted by formate ligands connecting three rod-shaped AlO_6 clusters through C-H···O interactions with a distance of 3.29 Å, exhibiting an unusual rod-based packing motif that is rarely observed among Al-based MOFs, with only two examples reported to date [24,25]. Crucially, structural analysis reveals that MOF-521 possesses a pore width of 7.23 Å and a confined pore volume of 0.60 $cm^3\ g^{-1}$. This precise dimension exquisitely matches the I_2 molecule, facilitating a dense self-assembly of intact I_2 molecules, as observed by single-crystal X-ray diffraction. This exact geometric matching yields an exceptional iodine packing density of 3.18 g cm^{-3}, approximately 65% pore-space utilization, and the ability to capture iodine at 120 ppm, verifying the effectiveness of physical confinement. Building on these mechanistic insights, we further investigate the role of pore modulation in regulating framework resilience and the reversibility of iodine storage. The rational post-synthetic modification using a ditopic fumarate linker to replace the original formate creates the first example of a **wwq** net found in MOF-521-Fum. The subtle architectural retrofitting expands the primary pore width from 7.23 Å to 7.85 Å and the overall pore volume to 0.71 $cm^3\ g^{-1}$. There is maintained yet a slight decline in the absolute packing density (to 2.79 g cm^{-3}), elegantly illustrating the sensitivity of guest confinement to pore geometry. Importantly, by overcoming structural fatigue during iodine desorption in MOF-521, the incorporation of fumarate enhances framework robustness and improves cycling stability under repeated iodine adsorption–desorption cycles. This work elucidates the physical constraints governing high density iodine storage and offers a structural fine-tuning approach to develop reversible and robust host-guest storage materials.

2 Experimental

2.1 Synthesis and activation of MOF-521

MOF-521 was synthesized via a solvothermal method with modified conditions. Aluminum chloride hexahydrate ($AlCl_3 \cdot 6H_2O$, 10.15 mg, 0.042 mmol, SCRC, 97%) and 1,3,5-tris(4-carboxyphenyl)benzene (H_3BTB, 12.415 mg, 0.0285 mmol, CHEMSOON, 98%) were dis-solved in 3 mL of *N*,*N*-diethylformamide (DEF), followed by the addition of 0.3 mL formic acid (HCOOH, SCRC, 98%). The solution was sonicated until completely dissolved and then transferred to a 10 mL Teflon-lined autoclave, which was heated at 160 °C for 24 h. The result-ing solid was washed three times with 10 mL *N*,*N*-dimethylformamide (DMF), followed by solvent exchange with acetone (3 × 10 mL/day) for three consecutive days. Finally, the sample was activated by evacuation at 120 °C under dynamic vacuum for 12 h.

2.2 Post-synthetic modification (PSM) of MOF-521 to MOF-521-Fum

MOF-521 (~15 mg) was dispersed in 10 mL DMF (generated by mixing 10 mg Fumaric acid) for 12 h at 100 °C, followed by solvent exchange with acetone (3 × 10 mL/day) for three consecutive days. Finally, the sample was activated by evacuation at 120 °C under dynamic vacuum for 12 h. The morphology of the crystals remains the same.

2.3 Single-crystal X-ray diffraction (SC-XRD)

SC-XRD data for the as-synthesized and iodine-loaded MOF-521 crystals were collected on a Bruker D8 Venture Photon III diffractometer using a Ga Kα source, or at the Shanghai Synchrotron Radiation Facility (BL17B, λ = 0.6701 Å; BL10U2, λ = 0.6887 Å).

2.4 Powder X-ray diffraction (PXRD)

PXRD patterns before and after iodine loading were recorded on a Bruker D8 Advance diffractometer with Cu Kα radiation (λ = 1.5418 Å) over a 2θ range of 3–30°, using a step size of 0.02° and a scan rate of $3°\cdot min^{-1}$.

2.5 Thermogravimetric analysis (TGA)

TGA was conducted on a PerkinElmer TGA 55 instrument at a heating rate of $10\ °C\cdot min^{-1}$ from room temperature to 700 °C under N_2 flow.

2.6 Raman spectroscopy

Raman spectra were acquired using an Andor SR 500I Raman spectrometer with 532 nm and 785 nm laser excitation sources. Spectra were recorded over the range 50 to 5000 cm^{-1} with 2 cm^{-1} resolution, accumulated over 1000 scans.

2.7 Scanning electron microscopy and energy dispersive X-ray spectroscopy (SEM-EDX)

SEM images were obtained using a JEOL JSM-7600F FE-SEM, and elemental mapping was performed with an Oxford Instruments X-Max 80 EDS system.

2.8 3D electron diffraction (3D-ED) data collection and processing

Sample was prepared according to the above method, loaded and transferred into the TEM to collect the 3D ED data. All 3D ED data were collected using a modified Instamatic

Just Accepted

software [26,27] on the TEM-JEM-F200 equipped with a hybrid-pixel electron detector (Cheetah 1800, 512 × 512 pixels, Amsterdam Scientific Instruments).

2.9 Diffuse reflectance UV-Vis spectroscopy

UV-vis spectra were recorded on a Varian Cary 5000 spectrometer using a Praying Mantis accessory. Data were collected in the 200-800 nm range with 1 nm resolution and presented via the Kubelka-Munk function.

2.10 X-ray photoelectron spectroscopy (XPS)

XPS was carried out using a Kratos Axis Ultra DLD spectrometer with a monochromated Al Kα source (1486.6 eV). Survey spectra were acquired at 80 eV pass energy; high-resolution spectra were recorded at 20 eV. Charge neutralization and ultrahigh vacuum (<3 × 10^{-8} mbar) were employed.

2.11 Static iodine vapor capture

Activated samples (pre-exchanged with acetone and evacuated at 120 °C for 3 days) were placed in a 4 mL sealed vessel containing solid iodine in an open vial. The sealed system was heated at 75 °C for vapor-phase iodine adsorption. The iodine uptake (M, g g^{-1}) was calculated using:

$$M=\frac{m_2-m_1}{m_1}\times 100\%$$

where m_1 and m_2 are the weights of the sample before and after iodine exposure, respectively [28].

2.12 Theoretical calculation

The RASPA software package [29] was used to perform Grand Canonical Monte Carlo (GCMC) simulations to generate the iodine adsorption sites. The frameworks are assumed to be rigid with fixed atoms in the grand canonical ensemble. The density-derived electrostatic and chemical method [30] was employed to calculate the net atom charges in the frameworks. CP2K software [31] was used for the Density Functional Theory (DFT) energy calculation to get the wave-function files and structure optimization using PBE12-D3(BJ) [32] exchange-correlation density functional with the DZVP-MOLOPT-SR-GTH basis set [33]. Interaction analyses using the independent gradient model based on the Hirshfeld partition of molecular density (IGMH) method were conducted with Multiwfn software [34,35].

3 Results and discussion

3.1 Molecular retrofitting of rod-packing MOF for enhanced stability

Pristine MOF-521 was obtained as colorless acicular crystals (Figure S1) suitable for SC-XRD analysis. SC-XRD reveals that MOF-521 crystallizes in the hexagonal P3c1 space group (No. 158) with the formula $C_{30}H_{18}Al_3O_{15}$. The unit cell parameters are a = b = 37.92(7) Å, c = 6.58(4) Å, and V = 8191 $Å^3$ (Figure S2, Table S1). This unique rod-based packing motif differs from previously reported Al-based rod MOFs (e.g., MIL-53(Al) [36], DUT-4 [37], A520 [38], Al-pyrMOF and Al-PMOF [39]). Topological analysis indicates that MOF-521 adopts the **etc** net, shown as its augmented rod net for clarity (Figure 1a) [40-42].

To achieve the expanded framework, direct de novo synthesis was extensively explored but consistently resulted in unknown amorphous phases (Figure S4). We hypothesize that the high rigidity and strong coordination affinity of fumarate ligands disrupt the formation of the original rod-shaped SBUs during framework nucleation, preventing the generation of the targeted architecture. Therefore, MOF-521-Fum was synthesized through a straightforward post-synthetic molecular retrofitting strategy, preserving the particle morphology (Figure S5). Quantitative liquid-state ^{1}H NMR of the acid-digested samples confirms the stoichiometric incorporation of fumarate and the complete disappearance of formate signals (Figures S6, S7). demonstrating a well-defined ligand exchange process rather than uncontrolled defect formation. Solid-state ^{13}C NMR further confirms a single, highly ordered coordination environment for the fumarate C=C bond, confirming the uniform incorporation of fumarate linkers within the framework (Figure S8).

Substituting a monodentate capping ligand with a rigid bridging ligand triggers a fundamental geometric rearrangement. Rather than simply occupying void space, fumarate chemically grafts at the junctions, connecting three adjacent SBUs. Acting as a rigid pillar, the dicarboxylic acid forcefully interlinks and separates the SBUs, driving a thermodynamic transition in the solid state to a more extended, open framework. The extensive structural reorganization during ligand substitution resulted in loss of single-crystal integrity, precluding direct analysis through single-crystal-to-single-crystal (SC–SC) transformation. Consequently, we determined the structure via a rigorous multi-technique cross validation. 3D-ED measurements provided the experimental unit-cell parameters of MOF-521-Fum, revealing an expanded crystalline lattice relative to MOF-521 (Figure S9, Table S3). Rietveld refinement of high-quality synchrotron PXRD data further showed that the proposed structural model is consistent with the experimental diffraction pattern and the unit-cell parameters determined by 3D-ED (Figure S10, Table S4). Combined with the ligand composition and stoichiometry established by ^{1}H and ^{13}C NMR, as well as the bridging coordination mode of fumarate, these results support the proposed framework connectivity. According to the RCSR convention, this connectivity corresponds to a previously unreported topology, which we denote herein as the **wwq** net (Figure 1a and Table S5). MOF-521-Fum thus represents, to the best of our knowledge, the first reported framework based on this topology, whose 2D projection corresponds to the **cpe** net (Figure S11) [40–42].

PXRD patterns of activated MOF-521 match the SC-XRD simulations, confirming phase purity (Figure 1b). In comparison, MOF-521-Fum retains a similar diffraction profile, while the main diffraction reflection exhibits a slight shift toward lower 2θ values, indicative of lattice expansion upon fumarate incorporation. To evaluate intrinsic porosity, N_2 adsorption isotherms were collected at 77 K. Following rigorous activation confirmed by TGA to eliminate desolvation artifacts, both materials exhibited characteristic type I microporous profiles. To-tal pore volumes increased from 0.60 cm^3 g^{-1} (MOF-521) to 0.71 cm^3 g^{-1} (MOF-521-

Just Accepted

Fum), with pore size distributions revealing a distinct expansion from 7.23 Å to 7.85 Å (Figure 1c). Supported by the expanded

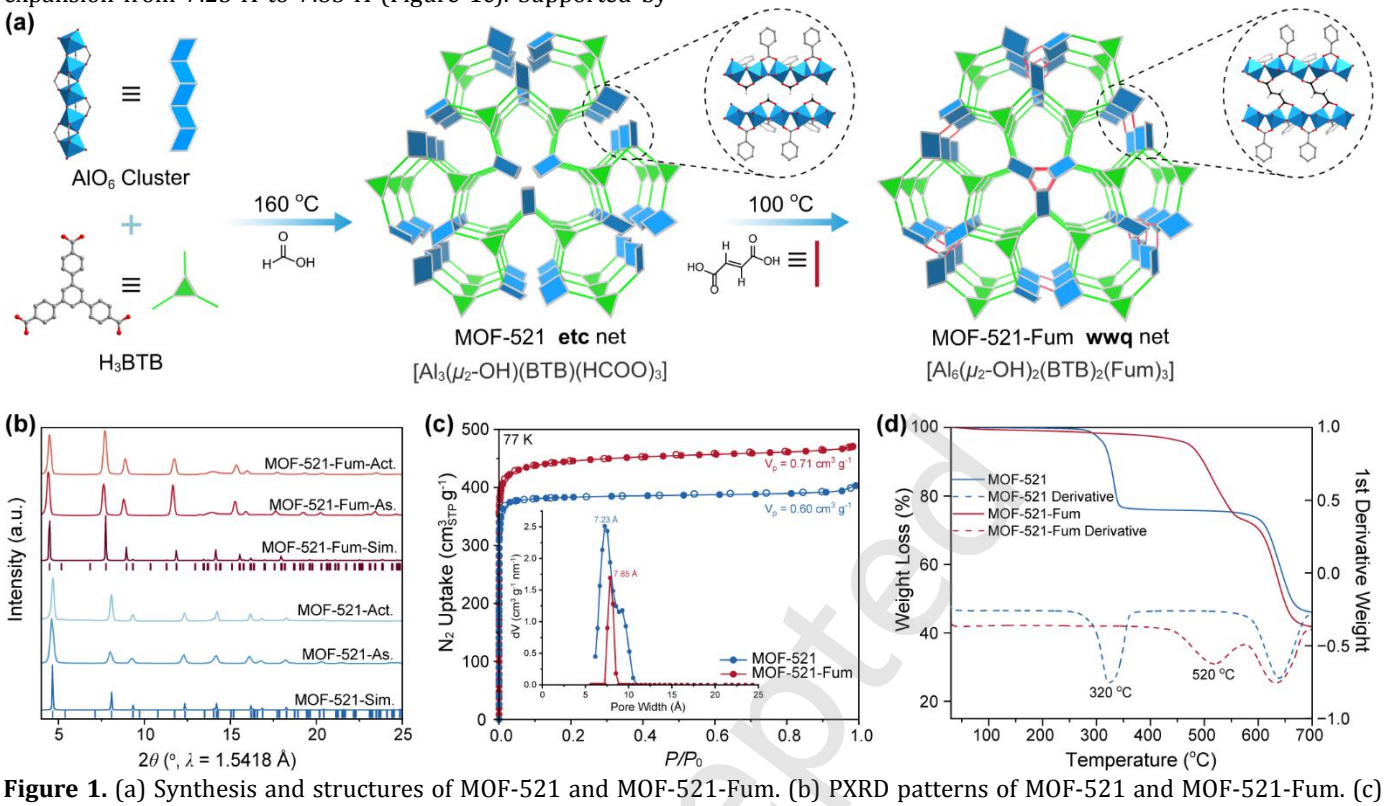

Figure 1. (a) Synthesis and structures of MOF-521 and MOF-521-Fum. (b) PXRD patterns of MOF-521 and MOF-521-Fum. (c) 77 K N_2 adsorption-desorption isotherms of MOF-521 and MOF-521-Fum. Inset: The pore size distribution of MOF-521 and MOF-521-Fum derived from their N_2 adsorption isotherms (d) TGA traces of MOF-521 and MOF-521-Fum under N_2 atmosphere.

crystallographic unit cell and stoichiometric NMR data, these results demonstrate that the enlarged pore space arises from defined ligand substitution within the framework rather than from uncontrolled defect generation. Furthermore, MOF-521-Fum exhibits high thermal stability, with framework decomposition occurring above ~500 °C (Figure 1d), highlighting the enhanced structural robustness imparted by fumarate incorporation.

3.2 Pore-geometry driven iodine assembly for high-capacity iodine uptake within confinement space

Capitalizing on the well-defined microporosity and intrinsic architectural stability of MOF-521 and its isoreticular analogue, MOF-521-Fum, we sought to exploit their 1D rhombic channels as precise nanoconfinement environments for iodine capture. To probe the intrinsic thermodynamic uptake limit and spatial packing efficacy, activated frameworks were exposed to iodine vapor at 75 °C under static conditions [43,44]. Both materials exhibited rapid initial iodine uptake, accompanied by a striking visual transition from colorless to opaque black, confirming dense guest incorporation (Figure 2a). SEM and elemental mapping confirm that the crystal morphology remains unchanged, with iodine homogeneously distributed throughout the bulk pores rather than aggregating on the surface (Figures S12–S13). Time-resolved PXRD further reveals the robust framework stability of MOF-521 during iodine confinement, as the characteristic diffraction features remain intact without detectable phase transformation (Figure S14). This confirms that iodine uptake proceeds through guest accommodation within the predefined channels rather than framework reconstruction.

The gravimetric uptake profiles revealed a pronounced initial adsorption stage within the first 10 h, followed by a gradual increase toward equilibrium capacities of 1.91 g g^{-1} for MOF-521 and 1.98 g g^{-1} for MOF-521-Fum after 30 h. To benchmark this spatial efficacy, we quantified the utilization of pore space for a series of representative iodine sorbents (Figure 2b, Table S6). MOF-521 achieved an exceptional pore-space utilization of ~65%, surpassing pristine benchmark MOFs without additional functionalization, including MFM-300(Sc) (62%), HKUST-1 (48%), MOF-808 (54%), MIL-101 (62%), UiO-66 (55%), and PCN-222 (48%). In comparison, MOF-521-Fum maintained a high utilization of 57% despite the expanded pore dimensions induced by fumarate incorporation. This comparative analysis corroborates our central hypothesis: the governing physical parameter for high density iodine storage is not merely the maximal pore volume, but rather the optimal pore geometry. The favorable geometric matching between the channel dimensions and I_2 molecules maximizes van der Waals potential overlap, promotes dense iodine organization and packing. Furthermore, we evaluated the reversibility of iodine release under a mild desorption condition (85 °C), which is essential for the practical utilization of iodine as a solid propellant in electric propulsion systems. MOF-521-Fum demonstrated a higher iodine release efficiency than MOF-521, delivering a ~21% enhancement in release efficiency over the full time course (Figure 2c). This enhanced reversibility highlights the importance of optimizing pore geometry to achieve both efficient iodine storage and reversible release.

Just Accepted

The beneficial effect of this structural modulation is most starkly manifested in the mechanical robustness of the frameworks during repeated adsorption–desorption cycling (Figure 2d). Pristine MOF-521 suffered rapid capacity degradation, retaining only ~20% of its initial uptake after 4th cycles. The structural deterioration underlying this capacity decay is supported by PXRD and N_2 sorption analyses

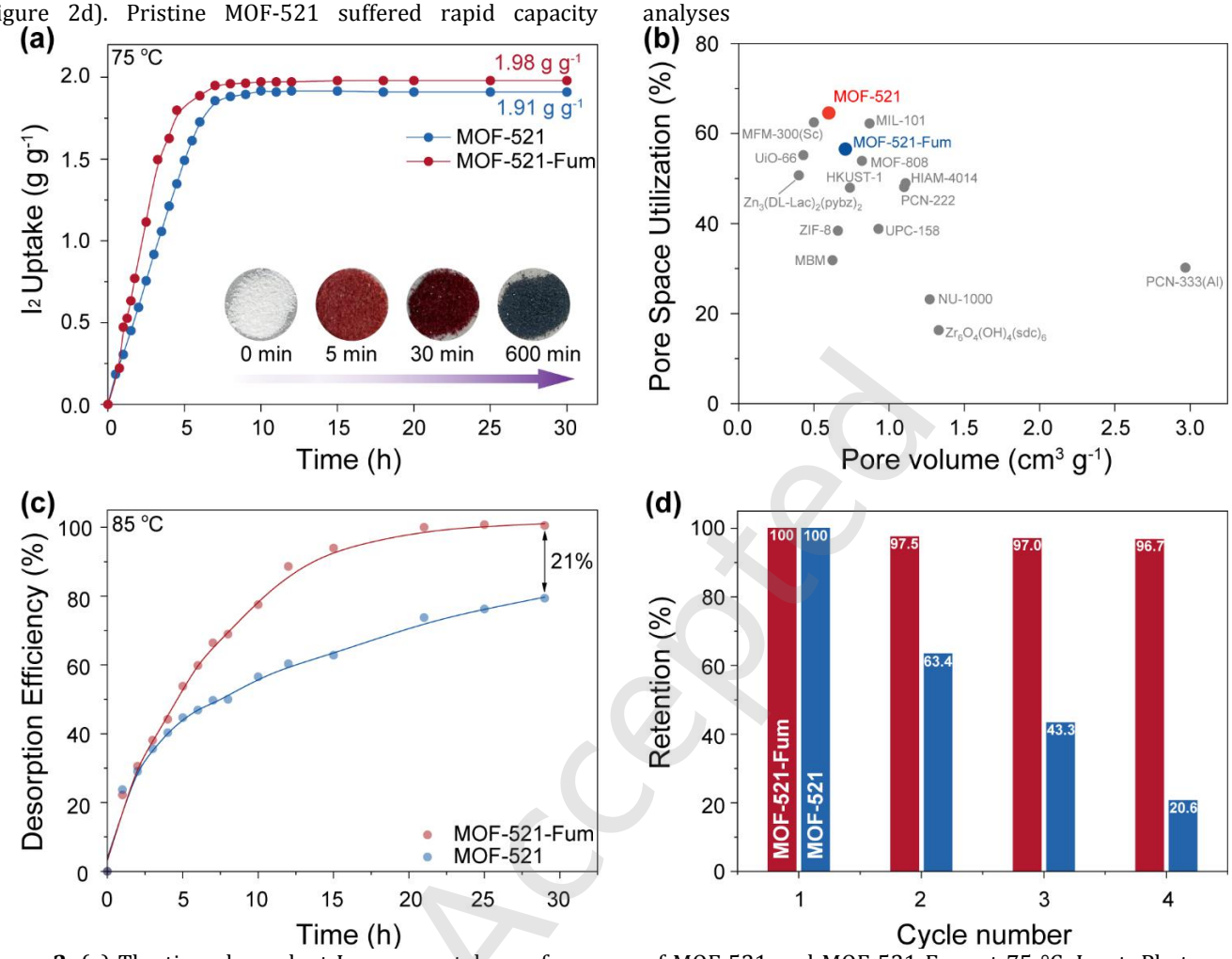

Figure 2. (a) The time-dependent I_2 vapor uptake performance of MOF-521 and MOF-521-Fum at 75 °C. Inset: Photographs showing the color evolution of MOF-521 crystals during adsorption. (b) Comparison of pore-space utilization versus pore volume for MOF-521 and MOF-521-Fum against representative, literature-reported I_2 sorbents. The comparative analysis exclusively evaluates representative frameworks exhibiting a baseline gravimetric adsorption capacity of approximately 1.0 g g^{-1} or greater. (c) I_2 desorption efficiency profiles at 85 °C. (d) Cyclic adsorption-desorption stability test over 4th cycles. Note: Pore space utilization is defined as the volume of confined I_2, calculated from the gravimetric uptake and the density of solid iodine, normalized to the total accessible pore volume of the framework.

(Figures S15-S16), which reveal severe amorphization and a catastrophic collapse of the permanent porosity due to framework fatigue under severe guest-loading stress. In sharp contrast, MOF-521-Fum retained >96% of its initial iodine uptake under identical conditions, flawlessly preserving its initial crystallinity and pore architecture. This demonstrates that judicious incorporation of fumarate fundamentally reinforces the lattice's structural resilience against cyclic guest-induced strain. Furthermore, the dense host-guest assembly within this confined space is macroscopically reflected by solid-state conductivity measure-ments. Upon iodine uptake, MOF-521 exhibits an approximately 200-folds enhancement in conductivity (from 3×10^{-6} to 6.4×10^{-4} S/cm). While the absolute conductivity remains modest relative to intrinsically conductive MOFs (Figure S17, Table S7), this dramatic two-order-of-magnitude enhancement strongly indicates that the restricted pore environment facilitates extended host-guest charge-transfer interactions, thereby generating new electron transport pathways.

To further validate the geometry-driven confinement hypothesis, the dynamic capture behavior and macroscopic electronic responses of these frameworks were evaluated. Under a continuous dilute iodine gas stream (~120 ppm), pristine MOF-521 exhibits a significantly prolonged initial breakthrough time (9.6 h) compared to the post-synthetically expanded MOF-521-Fum (9.0 h) (Figures S18–S20). The breakthrough curve of MOF-521-Fum displays a noticeably lower slope during the subsequent saturation phase. This slower saturation trajectory indicates that the expanded structural buffer provides a more favorable mass transfer zone and sustained dynamic retention capability. Subsequent TGA revealed weight losses of 6.0% and 7.0% for MOF-521 and MOF-521-Fum, respectively, corresponding to iodine uptake capacities of 0.06 g g^{-1} and 0.08 g g^{-1}. This performance demonstrates the potential of both frameworks to capture iodine at exceedingly low concentrations. Notably, among the materials evaluated

Just Accepted

under dynamic conditions at 120 ppm, only Pb-MOF-1 has been previously reported [21], yielding an uptake of 0.05 g g^{-1}.

3.3 Mechanistic insights into geometry-driven polyiodide assembly

To elucidate the fundamental host-guest interactions dictating this geometry-driven polyiodide assembly, MOF-521 and MOF-521-Fum were compared to evaluate their similarity in iodine confinement behavior.

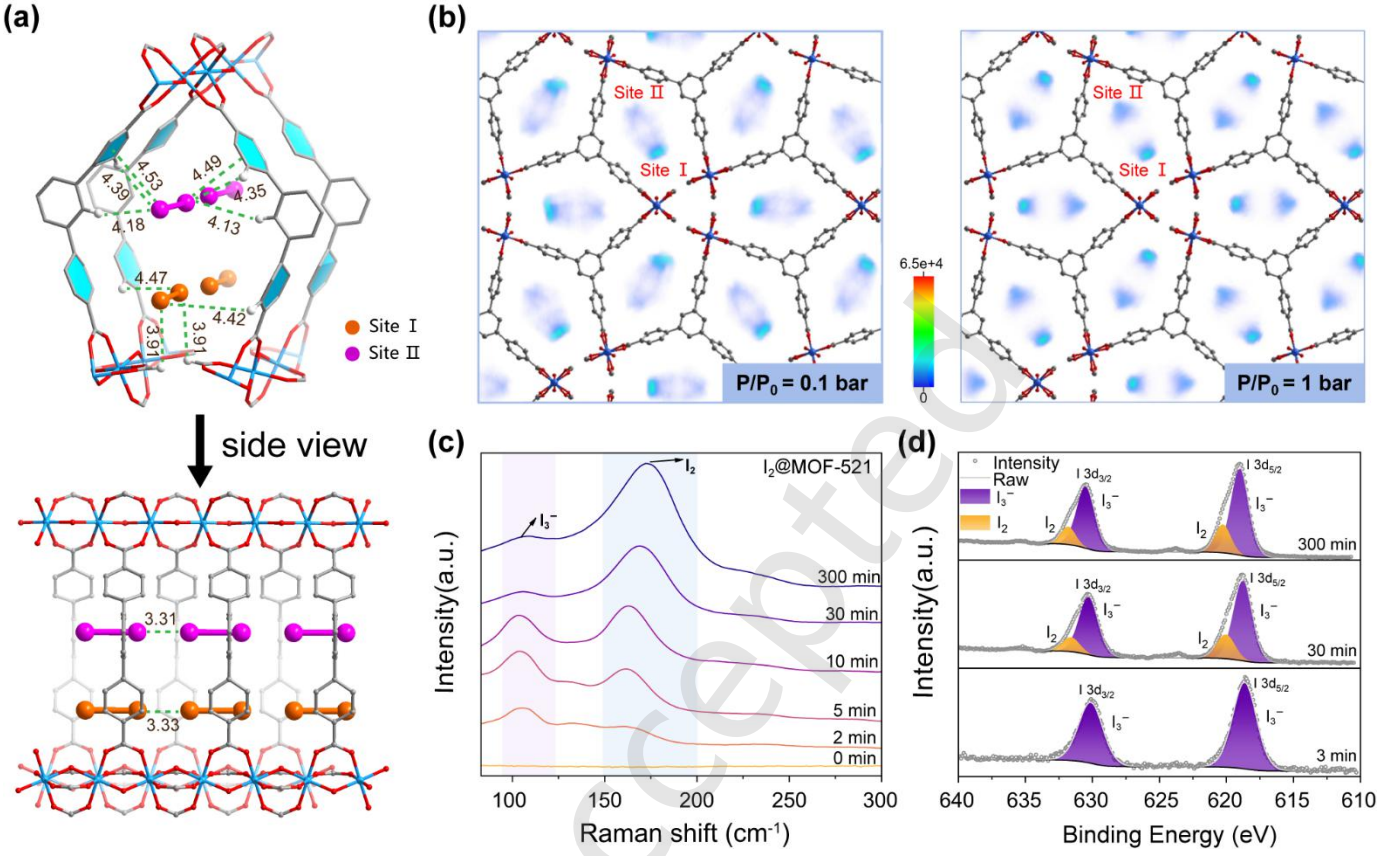

Figure 3. (a) Structural representation of iodine adsorption sites (Site I and Site II) within the framework channels. (b) GCMC-derived I_2 density distribution maps at different I_2 vapor pressures, illustrating the preferential occupation of Site I at lower pressure and the increased population of Site II upon further I_2 loading. (c) Raman of MOF-521 with different I_2-loaded amounts. (d) XPS spectra of I_2-loaded MOF-521.

Despite the accompanying changes in framework connectivity, pore dimensions, and rigidity, the broadly similar Raman and XPS signatures of I_2-loaded MOF-521 and MOF-521-Fum (Figures S21–S24), together with qualitatively similar iodine spatial distributions from GCMC simulations (Figure S25), indicate that their overall iodine confinement behavior remains broadly conserved. MOF-521 was therefore selected as a representative framework for detailed mechanistic investigation.

To gain atomic-level insight into this geometry-driven confinement, host–guest interactions were probed via SC-XRD of I_2-loaded MOF-521 (Figure S3, Table S2). Structural refinement confirms framework integrity ($C_{30}H_{18}Al_3O_{15}$), while the loaded crystal refined to a composition of $C_{30}H_{18}Al_3O_{15}I_{3.2}$. Because fully saturated iodine loading causes extreme X-ray absorption that degrades diffraction quality, the crystals were prepared after controlled iodine release at 75 °C for 3 h to ensure reliable atomic-level refinement. Due to the highly symmetric nature of the 1D channels and the dynamic mobility of the guests, the confined iodine species exhibit typical crystallographic positional disorder with fractional occupancies (ranging from 0.20 to 0.32). Despite this disorder, the SC-XRD analysis unambiguously identifies two primary, distinct binding domains (Figure 3a). Site I is localized near the formate groups of the Al-SBUs, showing a closest contact distance of 3.91 Å to the formate protons. Site II is located near the aromatic surfaces of the BTB linkers, with contacts to the phenyl rings in the 4.13–4.53 Å range, consistent with predominantly dispersive host–guest interactions. IGMH analysis (Figure S26) further corroborates that these host-guest interactions are dominated by dispersive interactions, without obvious evidence of strong directional host–guest interactions.

To further examine the spatial distribution of molecular iodine during pore filling, GCMC simulations were performed using a neutral MOF-521 framework and neutral I_2 molecules. The simulations show preferential occupation of the SBU-associated region at low loading, followed by increased population of other regions within the channel at higher loading (Figure 3b). Remarkably, this simulated progression is in precise agreement with the primary binding domains unambiguously identified by SC-XRD.

Raman spectroscopy elucidated the evolution of polyiodide species during iodine confinement. Pristine MOF-521 exhibits no background signals, confirming all observed peaks arise from adsorbed iodine (Figure 3c). The capture process uniquely evolves across two concentration regimes

Under Peer Review

via a proposed dual-stage synergistic mechanism. Stage I (Initial Iodine Organization): During the initial confinement process, iodine undergoes speciation evolution accompanied by partial charge redistribution, as suggested by the emergence of I_3^--related Raman features. This is evidenced by a prominent peak near 110 cm^{-1}, assigned to the symmetric and asymmetric stretching of framework-bound I_3^- [45,46]. Stage II (Geometry-Driven Physisorption): At higher iodine loading, the increasing band near 170 cm^{-1}, assigned to the I–I stretching of molecular I_2[47-49]. Time-dependent spectra reveal that the 110 cm^{-1} peak appears during the initial iodine accommodation stage, whereas the 170 cm^{-1} peak gradually increases at higher loadings, reflecting the evolution from locally stabilized iodine species to dense iodine assembly within the confined channels. XPS of vacuum pretreated samples corroborates this mechanism, confirming the coexistence of molecular I_2 (620.1/631.7 eV) and I_3^- (618.6/630.1 eV) [50] (Figure 3d). Because vacuum treatment removes loosely confined iodine species, XPS predominantly detects the more strongly retained iodine species within the framework, consistent with the Raman observations.

The high iodine packing density despite the absence of strong directional host–guest interactions highlights a synergistic interplay between spatial confinement and guest–guest cooperativity. The anisotropic 1D rhombic pores provide a geometrically constrained environment for iodine assembly. They strictly limit transverse thermal fluctuations while maximizing multidirectional van der Waals overlap. At higher loading, guest–guest interactions become increasingly important, favoring dense intermolecular organization within the confined channels. This is evidenced by the crystallographically observed axial I···I distances of 3.31 and 3.33 Å, which confirm the formation of continuous polyiodide chains.

4 Conclusions

In summary, we have established a geometry-driven confinement strategy to address trade-off between capacity and reversibility in metal–organic frameworks for iodine storage. By using MOF-521 as a model platform, we demonstrate that the precisely matched 1D rhombic channels with a pore width of 7.23 Å provide an ideal confined environment for iodine assembly, where geometric restriction maximizes van der Waals potential overlap and directs the formation of densely packed polyiodide chains. Comprehensive crystallographic, spectroscopic, and theoretical investigations reveal a stepwise iodine adsorption process, in which initial iodine-speciation evolution is followed by progressive physical filling and dense organization of iodine within the confined channels. While such confined packing favors high iodine storage, it also leads to structural deformation during iodine release, highlighting the need to balance guest packing with framework resilience. To address this limitation, molecular retrofitting of MOF-521 with rigid fumarate linkers affords MOF-521-Fum, in which modified pore dimensions and enhanced inter-SBU connectivity improve structural rigidity, retains high iodine storage and promote full iodine release. This work highlights pore geometry as an important spatial constraint for regulating iodine organization and packing, while framework connectivity provides an additional handle for improving structural stability and adsorption-release cyclicity, offering a general design consideration for balancing robustness, storage capacity and reversibility in porous materials.

Electronic Supplementary Material: Supplementary material (Synthetic details, single-crystal structural analysis, static gas/vapor adsorption isotherms, theoretical calculation, ^1H NMR spectroscopy, TGA, PXRD, SEM-EDX, XPS, and UV-vis spectra.) is available in the onlineversion of this article.

Data availability

All data needed to support the conclusions in the paper are presented in the manuscript and/or the Electronic Supplementary Material. Crystallographic data for the structures reported in this Article have been deposited at the Cambridge Crystallographic Data Centre under deposition numbers CCDC 2488109 (MOF-521), 2488108 (MOF-521-I_2) and 2576651 (MOF-521-Fum). Copies of the data can be obtained free of charge via https://www.ccdc.cam.ac.uk/structures/. Additional data related to this paper may be requested from the corresponding author upon request.

Acknowledgements

This work was supported by the National Natural Science Foundation of China (Nos. 22271189, 92356301, U23A2080, 22371173, and 22571187), the Science and Technology Commission of Shanghai Municipality (Nos. 21DZ2260400), and the ShanghaiTech AI4S Initiative (No. 2025AI4S04004). M.-H.Z. acknowledge the support from the BAGUI talent program (No. 2019AC26001), and the funding support from Scientific Research Initiation Grant in Shantou University (SRIG, NTF26016T). We thank Dr. N. Yu and L. Long at the Analytical Instrumentation Center (#SPST-AIC10112914) for technical support for XRD and adsorption measurements, and the HPC Platform of ShanghaiTech University for theoretical calculations. The authors thank the staff at the BL17B1 and BL10U2 beamlines of the National Facility for Protein Science in Shanghai and the Shanghai Synchrotron Radiation Facility of the Shanghai Advanced Research Institute, Chinese Academy of Sciences, respectively, for providing beam time and technical support during X-ray diffraction data collection. We thank Prof. Yanhang Ma and Dr. Shitao Wu from ShanghaiTech University for their assistance in 3D-ED. We thank Prof. Jiamin Xue and Dr. Qiyang Zhang from ShanghaiTech University for their assistance in the Electrical conductivity tests. We thank Dr. Lei Wei and Dr. Tengwu Zeng for their valuable discussions on the research work.

Declaration of competing interest

All the contributing authors report no conflict of interests in this work.

Author contribution statement

Y.Z., M.-H.Z. and Y.-B.Z. conceived, designed, and guided the project. W.W. carried out experiments, performed the data interpretation, and wrote the paper. W.Z., W.J., H.C., X.X., X.-D.W., and M.L. carried out experiments. Z.W. performed the theoretical calculations. Y.Zhao. edited the manuscript.

Use of AI statement

None.

References

[1] Mathew, M. D. Nuclear Energy: A Pathway towards Mitigation of Global Warming. Progr. *Nuclear Energy*. **2022**, *143*, 104080.

[2] Umadevi, K.; Mandal, D. Performance of Radio-Iodine

Not Accepted

Discharge Control Methods of Nuclear Reprocessing Plants. *J. Environ. Radioactivity*. **2021**, *234*, 106623.

[3] Levchenko, I.; Bazaka, K. Iodine powers low-cost engines for satellites. *Nature*. **2021**, *599*, 373−374.

[4] Rafalskyi, D.; Martinez, J.; Habl, L.; Rossi, E.; Proynov, P.; Bore, A.; Baret, T.; Poyet, A.; Lafleur, T.; Dudin, S.; Aanesland, A. In-orbit demonstration of an iodine electric propulsion system. *Nature*. **2021**, *599*, 411−415.

[5] Yaghi, O. M, M. J. Kalmutzki, C. S. Diercks, Introduction to Reticular Chemistry: Metal-Organic Frameworks and Covalent Organic Frameworks, *Wiley-VCH, Weinheim*. **2019**. 509pp.

[6] Zhang, X.; Maddock, J.; Nenoff, T. M.; Denecke, M. A.; Yang, S.; Schroder, M. Adsorption of Iodine in Metal-Organic Framework Materials. *Chem. Soc. Rev.* **2022**, *51*, 3243−3262.

[7] Pan, T.; Yang, K.; Dong, X.; Han, Y. Adsorption-Based Capture of Iodine and Organic Iodides: Status and Challenges. *J. Mater. Chem. A.* **2023**, *11*, 5460−5475.

[8] Li, X.; Pi, Y.; Tang, R.; Wang, X.; Wu, B.; Lin, F.; Tan, Y.; Ouyang, G. Charged Adsorbents for Iodine Capture. *Coord. Chem. Rev.* **2026**, *548*, 217148.

[9] Zeng, M.-H.; Wang, Q.-X.; Tan, Y.-X.; Hu, S.; Zhao, H.-X.; Long, L.-S.; Kurmoo, M. Rigid Pillars and Double Walls in a Porous Metal-Organic Framework: Single-Crystal to Single-Crystal, Controlled Uptake and Release of Iodine and Electrical Conductivity. *J. Am. Chem. Soc.* **2010**, *132*, 2561−2563.

[10] Sun, F.; Yin, Z.; Wang, Q.-Q.; Sun, D.; Zeng, M.-H.; Kurmoo, M. Tandem Postsynthetic Modification of a Metal–Organic Framework by Thermal Elimination and Subsequent Bromination: Effects on Absorption Properties and Photoluminescence. *Angew. Chem., Int. Ed.* **2013**, *52*, 4538−4543.

[11] Tao, Y.; Dong, Q.; Wan, J.; Huang, F.-P.; Duan, J.; Zeng, M.-H. Evolution from [Zn_9] to A Record-High [Zn_{54}] Subblock and Engineering a Hierarchical Supramolecular Framework for Enhanced Iodine Uptake. *Chem. Sci.* **2025**, *16*, 1730−1736.

[12] Sava, D. F.; Rodriguez, M. A.; Chapman, K. W.; Chupas, P. J.; Greathouse, J. A.; Crozier, P. S.; Nenoff, T. M. Capture of Volatile Iodine, a Gaseous Fission Product, by Zeolitic Imidazolate Framework-8. *J. Am. Chem. Soc.* **2011**, *133*, 12398−12401.

[13] Hughes, J. T.; Sava, D. F.; Nenoff, T. M.; Navrotsky, A. Thermochemical Evidence for Strong Iodine Chemisorption by ZIF-8. *J. Am. Chem. Soc.* **2013**, *135*, 16256−16259.

[14] Li, J.; Zhang, X.; Fan, M.; Chen, Y.; Ma, Y.; Smith, G. L.; Vitorica-yrezabal, I. J.; Lee, D.; Xu, S.; Schröder, M.; Yang, S. Direct Observation of Enhanced Iodine Binding within a Series of Functionalized Metal–Organic Frameworks with Exceptional Irradiation Stability. *J. Am. Chem. Soc.* **2024**, *146*, 14048−14057.

[15] Zhang, X.; da Silva, I.; Godfrey, H. G. W.; Callear, S. K.; Sapchenko, S. A.; Cheng, Y.; Vitorica-Yrezabal, I.; Frogley, M. D.; Cinque, G.; Tang, C. C.; Giacobbe, C.; Dejoie, C.; Rudic, S.; Ramirez-Cuesta, A. J.; Denecke, M. A.; Yang, S.; Schroder, M. Confinement of Iodine Molecules into Triple-Helical Chains within Robust Metal-Organic Frameworks. *J. Am. Chem. Soc.* **2017**, *139*, 16289−16296.

[16] Li, J.; Zhang, X.; Fan, M.; Chen, Y.; Ma, Y.; Smith, G. L.; Vitoricayrezabal, I. J.; Lee, D.; Xu, S.; Schröder, M.; Yang, S. Direct Observation of Enhanced Iodine Binding within a Series of Functionalized Metal–Organic Frameworks with Exceptional Irradiation Stability. *J. Am. Chem. Soc.* **2024**, *146*, 14048−14057.

[17] Han, Y.; He, Y.; Fu, Y.-K.; Huang, H.; Li, H.; Zhao, J.-P.; Wang, L.; Niu, Q.; Rosi, N. Crystallographic Visualization of Distinct Iodic Aggregations in Isostructural Metal−Organic Frameworks, *J. Am. Chem. Soc.* **2025**, *147*, 19968−19975.

[18] Song, A.-M.; Zhang, F.-D.; Peng, Z.-H.; Liang, R.-P.; Liao, J.-Z.; Ke, H.; Zhang, L.; Qiu, J.-D. Precise Identification of Radioactive Iodine within Interlayer Molecular Cages of Metal–Organic Frameworks, *J. Am. Chem. Soc.* **2025**, *147*, 32352−32356.

[19] Zhang, Z.; Dong, X.; Yin, J.; Li, Z.-G.; Li, X.; Zhang, D.; Pan, T.; Lei, Q.; Liu, X.; Xie, Y.; Shui, F.; Li, J.; Yi, M.; Yuan, J.; You, Z.; Zhang, L.; Chang, J.; Zhang, H.; Li, W.; Fang, Q.; Li, B.; Bu, X.-H.; Han, Y. Chemically Stable Guanidinium Covalent Organic Framework for the Efficient Capture of Low-Concentration Iodine at High Temperatures. *J. Am. Chem. Soc*. **2022**, *144*, 6821−6829.

[20] Liu, X.; Zhang, Z.; Zhang, S.; Li, L.; Wang, J.; Shui, F.; Yi, M.; You, Z.; Wang, S.; Liu, Y.; Zhao, Q.; Li, B.; Bu, X-H. Pore Space Multi-Layer Functionalization Boosting Industrial Radioactive Iodine Capture with Record Capacity and Exceptional Kinetics, *Angew. Chem., Int. Ed.* **2026**, *65*, e21492.

[21] Yu, Y.-N.; Ma, W.-M.; Wu, J.-X.; Zhang, Q.; Zhou, J.; Jiang, K.-K.; Wang, D.-D.; Li, Y.-K.; Ma, Y.-M.; Yin, Z. Efficient Capture of Gaseous, Aqueous Iodine, Near-Sunlight White Light Emission and Iodine Sensing in 12-Connected and $[Pb_6]^{-}$ Cluster Based MOFs. *Chem. Eng. J.* **2025**, *504*, 158782.

[22] Zhang, J.; Wang, X.; Guo, X.; Sang, W.; He, Q.; Zhang, W. Crystal- and Pore-Size Dependent Iodine Adsorption Properties in MOFs. *Small.* **2025**, *21*, 2410678.

[23] Wang, D.; Guo, W.; Hu, J.; Liu, F.; Chen, L.; Du, S.; Tang, Z. Estimating Atomic Sizes with Raman Spectroscopy. *Sci. Rep.* **2013**, *3*, 1486.

[24] Zheng, Z.; Rong, Z.; Rampal, N.; Borgs, C.; Chayes, J. T.; Yaghi, O. M. A GPT-4 Reticular Chemist for Guiding MOF Discovery. *Angew. Chem., Int. Ed.* **2023**, *62*, e202311983.

[25] Hu, L.; Wu, W.; Gong, L.; Zhu, H.; Jiang, L.; Hu, M.; Lin, D.; Yang, K. A Novel Aluminum-Based Metal-Organic Framework with Uniform Micropores for Trace BTEX Adsorption. *Angew. Chem., Int. Ed.* **2023**, *62*, e202215296.

[26] Wang, B.; Zou, X.; Smeets, S. Automated serial rotation electron diffraction combined with cluster analysis: an efficient multi-crystal workflow for structure determination. *IUCrJ.* **2019**, *6*, 854−867.

[27] Ling, Y.; Sun, T.; Guo, L.; Si, X.; Jiang, Y.; Zhang, Q.; Chen, Z.; Terasaki, O.; Ma, Y. Atomic-level structural responsiveness to environmental conditions from 3D electron diffraction. *Nat. Commun.* **2022**, *13*, 6625.

[28] Xiao, C.; Tian, J.; Jiang, F.; Yuan, D.; Chen, Q.; Hong, M. Optimizing Iodine Enrichment through Induced-Fit Transformations in a Flexible Ag(I)-Organic Framework: From Accelerated Adsorption Kinetics to Record-High Storage Density. *Small* **2024**, *20*, 2311181.

[29] Dubbeldam, D.; Calero, S.; Ellis, D. E.; Snurr, R. Q. RASPA: Molecular Simulation Software for Adsorption and Diffusion in Flexible Nanoporous Materials. *Mol. Simul.* **2016**, *42*, 81−101.

[30] Manz, T. A.; Limas, N. G. Introducing Ddec6 Atomic Population Analysis: Part 1. Charge Partitioning Theory and Methodology. *RSC Adv.* **2016**, *6*, 47771−47801.

[31] Kühne, T. D.; Iannuzzi, M.; Del Ben, M.; Rybkin, V. V.; Seewald, P.; Stein, F.; Laino, T.; Khaliullin, R. Z.; Schütt, O.; Schiffmann, F. CP2K: An Electronic Structure and Molecular Dynamics Software Package-Quickstep: Efficient and Accurate Electronic Structure Calculations. *J. Chem. Phys.* **2020**, *152.*

[32] Grimme, S.; Ehrlich, S.; Goerigk, L. Effect of The Damping Function in Dispersion Corrected Density Functional Theory. J. *Comput. Chem.* **2011**, *32*, 1456−1465.

[33] VandeVondele, J.; Hutter, J. Gaussian Basis Sets for Accurate Calculations on Molecular Systems in Gas and Condensed Phases. *J. Chem. Phys.* **2007**, *127*, 114105

[34] Lu, T.; Chen, F. Multiwfn: A Multifunctional Wavefunction Analyzer. *J. Comput. Chem.* **2012**, *33*, 580−592.

[35] Lu, T.; Chen, Q. Independent Gradient Model Based on Hirshfeld Partition: A New Method for Visual Study of Interactions in Chemical Systems. *J. Comput. Chem.* **2022**, *43*, 539−555.

[36] Loiseau, T.; Serre, C.; Huguenard, C.; Fink, G.; Taulelle, F.; Henry, M.; Bataille, T.; Férey, G. A Rationale for the Large Breathing of the Porous Aluminum Terephthalate (MIL-53) Upon Hydration. *Chem. Eur. J.* **2004**, *10*, 1373−1382.

[37] Reinsch, H.; Krüger, M.; Wack, J.; Senker, J.; Salles, F.; Maurin, G.; Stock, N. A New Aluminium-Based Microporous Metal–Organic Framework: Al(BTB) (BTB=1,3,5-Benzenetrisbenzoate). Microporous *Mesoporous Mater.* **2012**, *157*, 50−55.

[38] Alvarez, E.; Guillou, N.; Martineau, C.; Bueken, B.; van de

Just Accepted

Voorde, B.; Le Guillouzer, C.; Fabry, P.; Nouar, F.; Taulelle, F.; de Vos, D. The Structure of the Aluminum Fumarate Metal–Organic Framework A520. *Angew. Chem., Int. Ed.* **2015**, *54*, 3664−3668.

[39] Boyd, P. G.; Chidambaram, A.; García-Díez, E.; Ireland, C. P.; Daff, T. D.; Bounds, R.; Gładysiak, A.; Schouwink, P.; Moosavi, S. M.; Maroto-Valer, M. M.; Reimer, J. A.; Navarro, J. A. R.; Woo, T. K.; Garcia, S.; Stylianou, K. C.; Berend, S. Data-Driven Design of Metal–Organic Frameworks for Wet Flue Gas CO_2 Capture. *Nature.* **2019**, *576*, 253−256.

[40] O'Keeffe, M.; Peskov, M. A.; Ramsden, S. J.; Yaghi, O. M. The Reticular Chemistry Structure Resource (RCSR) Database of, and Symbols for, Crystal Nets. *Acc. Chem. Res.* **2008**, *41*, 1782−1789.

[41] Li, M.; Li, D.; O'Keeffe, M.; Yaghi, O. M. Topological Analysis of Metal−Organic Frameworks with Polytopic Linkers and/or Multiple Building Units and the Minimal Transitivity Principle. *Chem. Rev.* **2014**, *114*, 1343−1370.

[42] Schoedel, A.; Li, M.; Li, D.; O'Keeffe, M.; Yaghi, O. M. Structures of Metal–Organic Frameworks with Rod Secondary Building Units. *Chem. Rev.* **2016**, *116*, 12466−12535.

[43] Lin, Y.; Zeng, P.; Wang, D.; Li, T.-T.; Wu, L.-H.; Zheng, S.-R. A Mixed-Ligand Co(II) MOF Synthesized from A Single Organic Ligand to Capture Iodine and Methyl Iodide Vapour. *Dalton Trans.* **2023**, *52*, 7709−7717.

[44] Small, L. J.; Hill, R. C.; Krumhansl, J. L.; Schindelholz, M. E.; Chen, Z.; Chapman, K. W.; Zhang, X.; Yang, S.; Schroder, M.; Nenoff, T. M. Reversible MOF-Based Sensors for the Electrical Detection of Iodine Gas. *ACS Appl. Mater. Interfaces*. **2019**, *11*, 27982−27988.

[45] Deplano, P.; Devillanova, F. A.; Ferraro, J. R.; Mercuri, M. L.; Lippolis, V.; Trogu, E. F. FT-Raman Study on Charge-Transfer Polyiodide Complexes and Comparison with Resonance Raman Results. *Appl. Spectro.* **1994**, *48*, 1236−1241.

[46] Andrade, P. H. M.; Ahouari, H.; Volkringer, C.; Loiseau, T.; Vezin, H.; Hureau, M.; Moissette, A. Electron-Donor Functional Groups, Band Gap Tailoring, and Efficient Charge Separation: Three Keys to Improve the Gaseous Iodine Uptake in MOF Materials. *ACS Appl. Mater. Interfaces.* **2023**, *15*, 31032−31048.

[47] Lee, B.; Chen, Y.-P.; Park, J.; Park, J. Visualization of Iodine Chemisorption Facilitated by Aryl C–H Bond Activation. *ACS Appl. Mater. Interfaces.* **2019**, *11*, 25817−25823.

[48] Maddock, J.; Kang, X.; Liu, L.; Han, B.; Yang, S.; Schröder, M. The Impact of Structural Defects on Iodine Adsorption in UiO-66. *Chemistry*. **2021**, *3*, 525-531.

[49] Qasem, K. M. A.; Khan, S.; Ahamad, M. N.; Saleh, H. A. M.; Ahmad, M.; Shahid, M. Radioactive Iodine Capture by Metal Organic Frameworks in Liquid and Vapour Phases: An Experimental, Kinetic and Mechanistic Study. *J. Environ. Chem. Eng.* **2021**, *9*, 106720.

[50] Gonzalez-Juarez, M. d. L.; Isaacs, M. A.; Bradshaw, D.; Nandhakumar, I. Enhanced Thermoelectric Properties of a Semiconducting Two-Dimensional Metal–Organic Framework via Iodine Loading. *ACS Appl. Mater. Interfaces*. **2023**, *15*, 5478−5486.

© The Author(s) 2026. *Nano Research* published by Tsinghua University Press. The articles published in this open access journal are distributed under the terms of the Creative Commons Attribution 4.0 International License (http://creativecommons.org/licenses/by/4.0/), which permits use, distribution and reproduction in any medium, provided the original work is properly cited.

Just Accepted

Electronic Supplementary Material

Geometry-driven confinement and iodine evolution in robust metal–organic frameworks for adsorptive iodine storage

Wenqi Wang[1], Weixiang Zuo[1], Zhe Wang[1], Wentao Jiang[1], Hao Chen[1], Xinyi Xu[1], Xu-Dong Wu[3], Mian Li[3], Yingbo Zhao[1], Zheng Yin[2] ✉, Ming-Hua Zeng[2,3] ✉, and Yue-Biao Zhang[1] ✉

[1] *Institute of Carbon Neutrality, School of Physical Science and Technology, Shanghai Key Laboratory of High-Resolution Electron Microscopy, and State Key Laboratory of Advanced Medical Materials and Devices, ShanghaiTech University, Shanghai 201210, China*
[2] *Key Laboratory for Chemistry and Molecular Engineering of Medicinal Resources (Ministry of Education of China), Guangxi Key Laboratory of Chemistry and Molecular Engineering of Medicinal Resources, School of Chemistry and Pharmaceutical Sciences, Guangxi Normal University, Guilin 541004, China*
[3] *College of Chemistry and Chemical Engineering, Key Laboratory for Preparation and Application of Ordered Structural Materials of Guangdong Province, Shantou University, Guangdong 515063, China*

✉Address correspondence to Zheng Yin, yinzheng@mailbox.gxnu.edu.cn; Ming-Hua Zeng, zmh@mailbox.gxnu.edu.cn; Yue-Biao Zhang, zhangyb@shanghaitech.edu.cn

Supporting information to https://doi.org/10.26599/NR.2026.94909258

Just Accepted

Address correspondence to Zheng Yin, yinzheng@mailbox.gxnu.edu.cn; Ming-Hua Zeng, zmh@mailbox.gxnu.edu.cn; Yue-Biao Zhang zhangyb@shanghaitech.edu.cn

Section S1. Synthesis and Characterization

Materials. Aluminum chloride hexahydrate [$AlCl_3 \cdot 6H_2O$] (purity > 97.0%) was purchased from Sinopharm Chemical Reagent Co.; 1,3,5-tris(4-carboxyphenyl)benzene [H_3BTB] (purity > 98.0%) was purchased from CHEMSOON Co. All the starting materials mentioned above were used as received without further purification. *N*,*N*-diethylformamide (DEF) was purchased from Bainiannuan Sci.&Tec. Co.; *N*,*N*-dimethylformamide (DMF) was purchased from Aladdin BioChem Tech. Co.; Acetone (AC) was purchased from Sinopharm Chemical Reagent Co.; Formic acid (HCOOH) was purchased from Sinopharm Chemical Reagent Co.

Synthesis and activation of MOF-521 [$Al_3(\mu_2\text{-}OH)(BTB)(HCOO)_3$]. A mixture of $AlCl_3 \cdot 6H_2O$ (10.15 mg, 0.042 mmol), H_3BTB (12.415 mg, 0.0285 mmol) was dissolved in DEF (3 ml), The solution was sonicated until complete dissolution and then transferred to a 10 mL Teflon-lined autoclave, which was heated at 160 °C for 24 h. Transparent needle-shaped crystals were collected and washed with fresh DMF for 3 times (named MOF-521-as), followed by solvent exchange with acetone (3 × 10 mL/day) for three consecutive days until the elimination of DMF in MOFs is monitored by NMR spectroscopy of digested solutions. Finally, the sample was activated by evacuation at 120 °C overnight on a FLOVAC activation station from Quantachrome.

Post-synthetic conversion of MOF-521 to MOF-521-Fum [$Al_6(\mu_2\text{-}OH)(BTB)_2(Fum)_3$]. MOF-521 (~15 mg) was dispersed in 10 ml DMF (generated by mixing 10 mg Fumaric acid) for 12 h at 100 °C. Transparent needle-shaped crystals were collected and washed with fresh DMF for 3 times (named MOF-521-as) and followed by solvent exchange with acetone (3 × 10 mL/day) for three consecutive days until the elimination of DMF in MOFs was monitored by NMR spectroscopy of digested solutions. Finally, the sample was activated by evacuation at 120 °C overnight on a FLOVAC activation station from Quantachrome.

Characterization and Instrumentation. The phase purity and crystallinity of MOF-521 were determined with a powder X-ray diffractometer (Bruker, D8 Advance, Cu Kα). The crystal size and morphology were examined using a scanning electron microscope (Phenom-World BV, Prox). Thermogravimetric analyses (TGA) were performed on a TGA instrument (PerkinElmer TGA 55) with a heating rate of 10 °C·min-1 from ambient temperature to 700 °C under N2 flow. Raman spectra were collected on a Raman spectrometer (Andor SR 500I). The formula of the activated MOFs was confirmed by their digested-solution 1H nuclear magnetic resonance (NMR) spectra, which were collected on a Bruker AVANCE NEO 400 (400 MHz) NMR spectrometer, with Deuterium Dimethyl Sulfoxide as deuterium reagent. Solid-state 1H nuclear magnetic resonance (SSNMR) spectroscopy is performed using magic angle spinning (MAS) on a Bruker AVANCE III HD 400 MHz wide-bore solid-state NMR spectrometer at a magnetic field of 9.4 T, equipped with a standard Bruker MAS probe and a 3.2 mm (o.d.) zirconia rotor. All 1H NMR spectra were acquired using a standard 3.2 mm double-resonance probe at a sample spinning rate of 12 kHz. The 1H chemical shifts are calibrated by the hydrogen of the adamantane reference sample assigned to 1.91 ppm.

Just Accepted



Figure S1. The optical microscope image of as-synthesized crystals of MOF-521.

Just Accepted

Section S2. Single-Crystal X-ray Diffraction analyses

Data collection. Single-crystal X-ray diffraction (SC-XRD) data of MOF-521 and MOF-521-I2 were collected at Shanghai Synchrotron Light Source Line BL17B station (λ = 0.6705 or 0.6887 Å) equipped with a marXperts MX300 CCD detector.

Structure solution and refinement. All the crystal structures were solved by direct methods using the SHLEXL software package and further developed with different Fourier syntheses. All non-hydrogen atoms were refined anisotropically, and all hydrogen atoms were added geometrically and refined in the riding model. All the aromatic rings were refined with rigid constraints, and the occupancies of disordering sets were refined using free variables.

Note. During the crystallographic structure refinement, guest iodine atoms confined within the MOF channels were located near special high-symmetry positions (mirror planes and two-fold axes). Consequently, symmetry operations generated equivalent atomic sites with unphysically short interatomic distances (~1.6 Å). This strictly reflects the spatial and temporal statistical averaging of highly disordered guest molecules across the macroscopic crystal lattice, rather than actual short-range physical interactions. To accurately resolve this artifact, the PART -1 instruction was implemented. The disordered iodine atoms were assigned partial occupancies, correctly defining them as mutually exclusive within any single unit cell. For clarity in structural visualizations and to depict a realistic local chemical environment, only one representative set of these disordered positions is displayed.

Crystallographic data have been deposited in the Cambridge Crystallographic Data Center, as CCDC 2488109 (MOF-521) and 2488108 (MOF-521-I2). These data can be obtained free of charge via www.ccdc.cam.ac.uk/data_request/cif.

Just Accepted

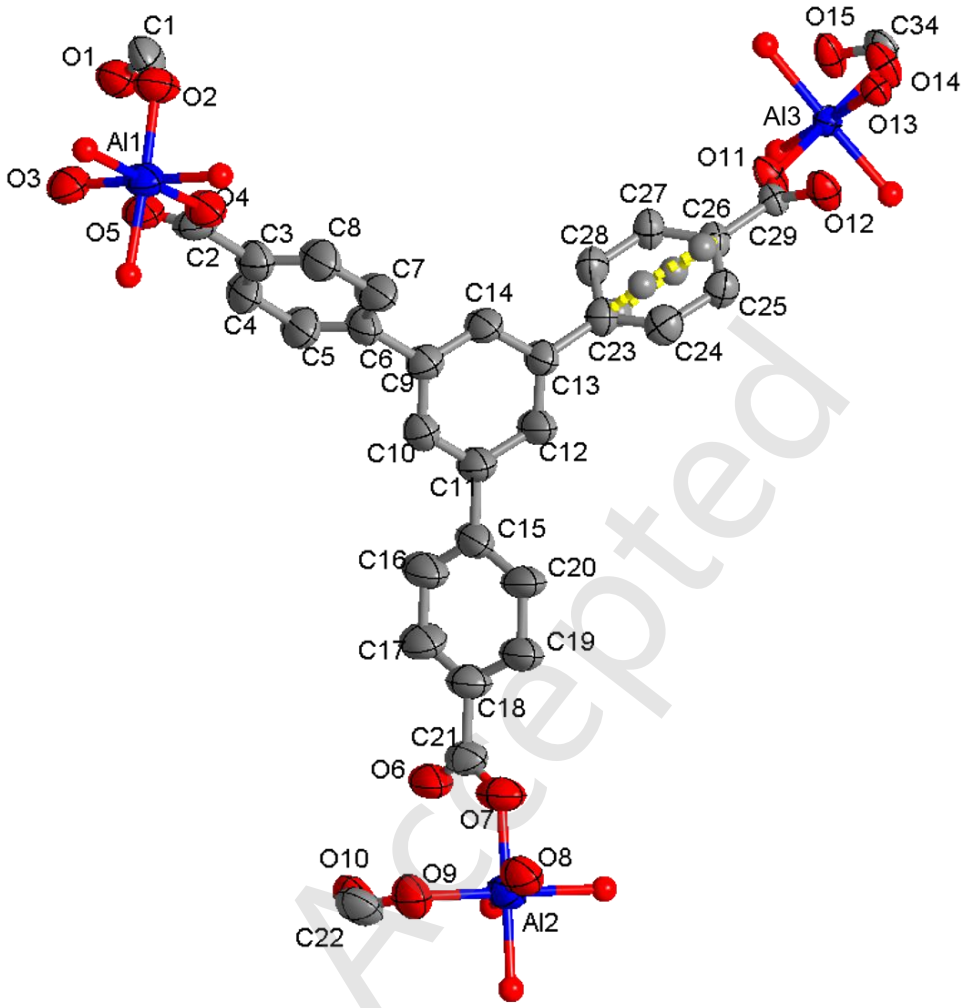

Figure S2. Asymmetric unit in the single crystal structure of MOF-521 (thermal ellipsoids with 30% probability; carbon, grey; aluminium, blue; oxygen, red). Hydrogen atoms are omitted for clarity. Orange bonds represent the disordering of BTB. Symmetry-related atoms are not labeled and represented as spheres.

Just Accepted

Table S1. Crystallographic data and structural determination of MOF-521.

Compound	**MOF-521**
Chemical formula	$C_{30}H_{18}O_{15}Al_3$
Formula mass	699.38
Crystal system	Trigonal
Space group	*P*3*c*1 (**No**.158)
λ (Å)	0.6887
a (Å)	37.9237(7)
c (Å)	6.5764(4)
γ (°)	120
V (Å^3)	8190.6(9)
Z	6
T (K)	100
$d_{crystal}$ (g/cm^3)	0.851
Measured reflections	10835
Unique reflections	7042
Parameters	472
Restraints	245
R_{int}	0.0999
θ range (°)	2.75 – 25.51
R_1, wR_2	0.0688, 0.2202
S (GOF)	1.088
Max/min residual density (e/Å^3)	+0.429 / -0.383

$^aR_1 = \sum ||F_o| - |F_c|| / \sum |F_o|$; $^bwR_2 = \left[\sum w(F_o^2 - F_c^2)^2 / \sum w(F_o^2)^2\right]^{1/2}$; $^cS = \left[\sum w(F_o^2 - F_c^2)^2 / (N_{ref} - N_{par})\right]^{1/2}$.

Just Accepted

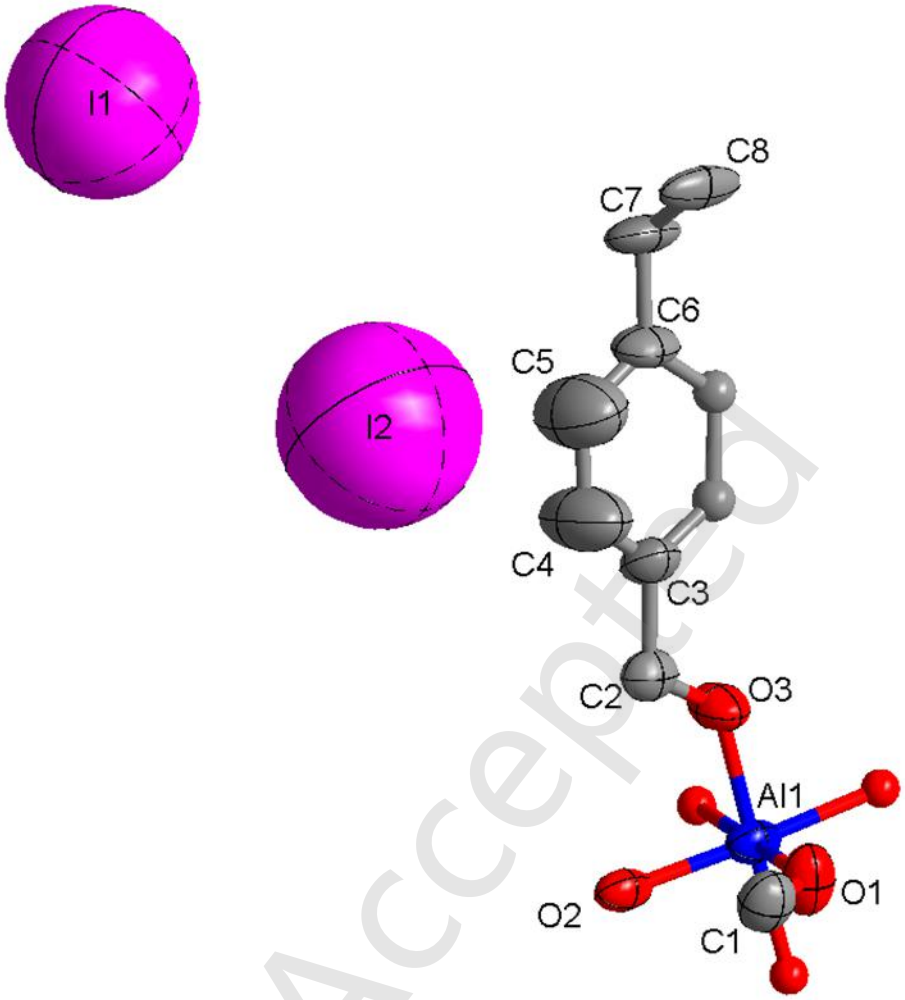

Figure S3. Asymmetric unit in the single crystal structure of MOF-521-I_2 (thermal ellipsoids with 30% probability; carbon, grey; aluminium, blue; oxygen, red). Hydrogen atoms are omitted for clarity. Orange bonds represent the disordering of BTB. Symmetry-related atoms are not labeled and represented as spheres.

Just Accepted

Table S2. Crystallographic data and structural determination of MOF-521-I_2.

Compound	**MOF-521-I_2**
Chemical formula	$C_{30}H_{18}O_{15}Al_3I_{3.16}$
Formula mass	1099.75
Crystal system	Hexagonal
Space group	$P\bar{6}2c$ (**No**.190)
λ (Å)	0.6887
a (Å)	21.961 (4)
c (Å)	6.6238 (3)
γ (°)	120
V (Å^3)	2766.3 (3)
Z	2
T (K)	100
$d_{crystal}$ (g/cm^3)	1.320
Measured reflections	1074
Unique reflections	921
Parameters	124
Restraints	75
R_{int}	0.0948
θ range (°)	1.797 – 20.118
R_1, wR_2	0.0860, 0. 2470
S (GOF)	1.088
Max/min residual density (e/Å^3)	+0.535 / -0.383

$^aR_1 = \sum ||F_o| - |F_c|| / \sum |F_o|$; $^bwR_2 = \left[\sum w(F_o^2 - F_c^2)^2 / \sum w(F_o^2)^2\right]^{1/2}$; $^cS = \left[\sum w(F_o^2 - F_c^2)^2 / (N_{ref} - N_{par})\right]^{1/2}$.

Just Accepted

Section S3. Post-Synthetic Modification and Morphological Integrity

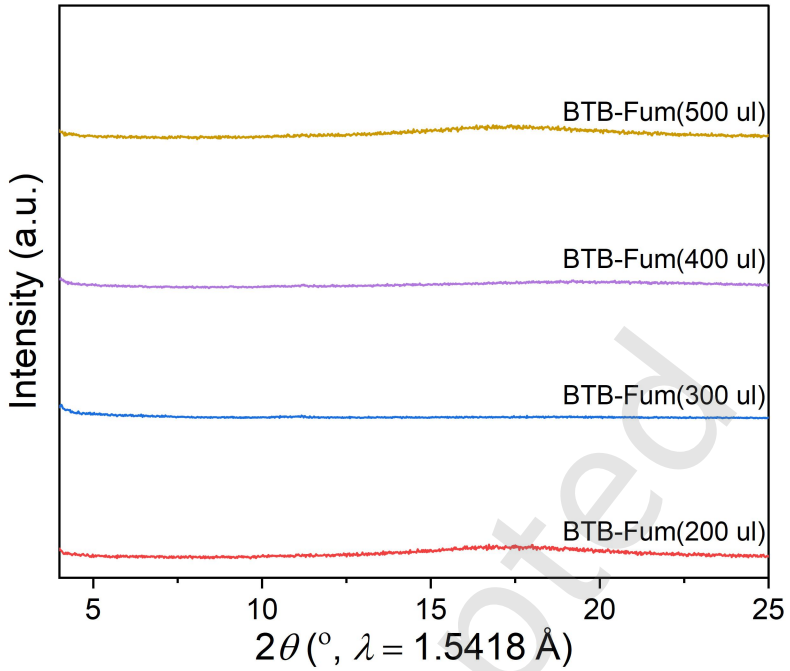

Figure S4. PXRD pattern of products synthesized via a one-pot strategy for MOF-521-Fum, with a fixed amount of BTB linker and varying volumes of fumaric acid (Fum).

Just Accepted

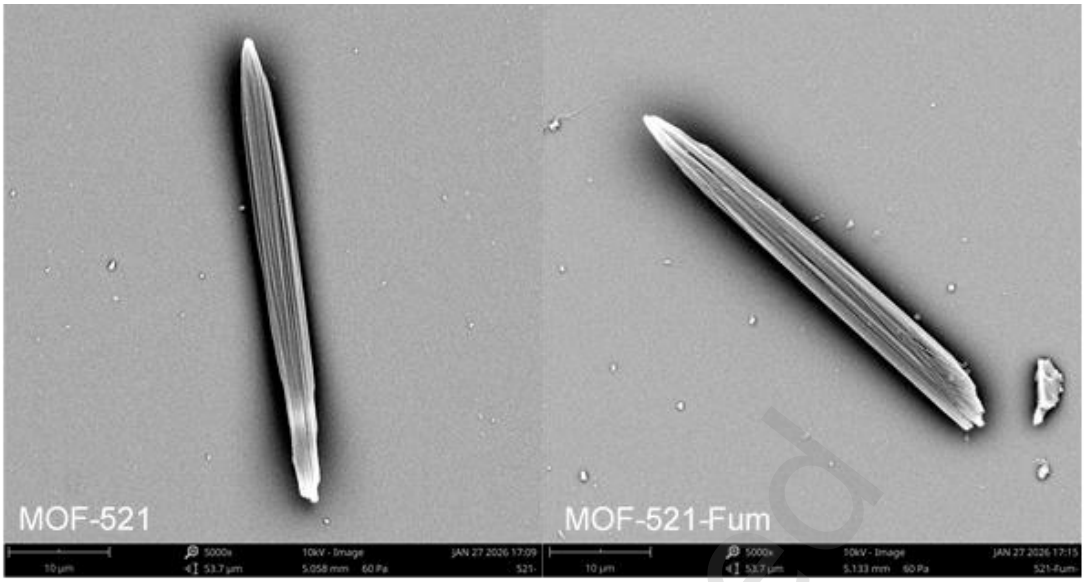

Figure S5. SEM images of MOF-521 and MOF-521-Fum.

Just Accepted

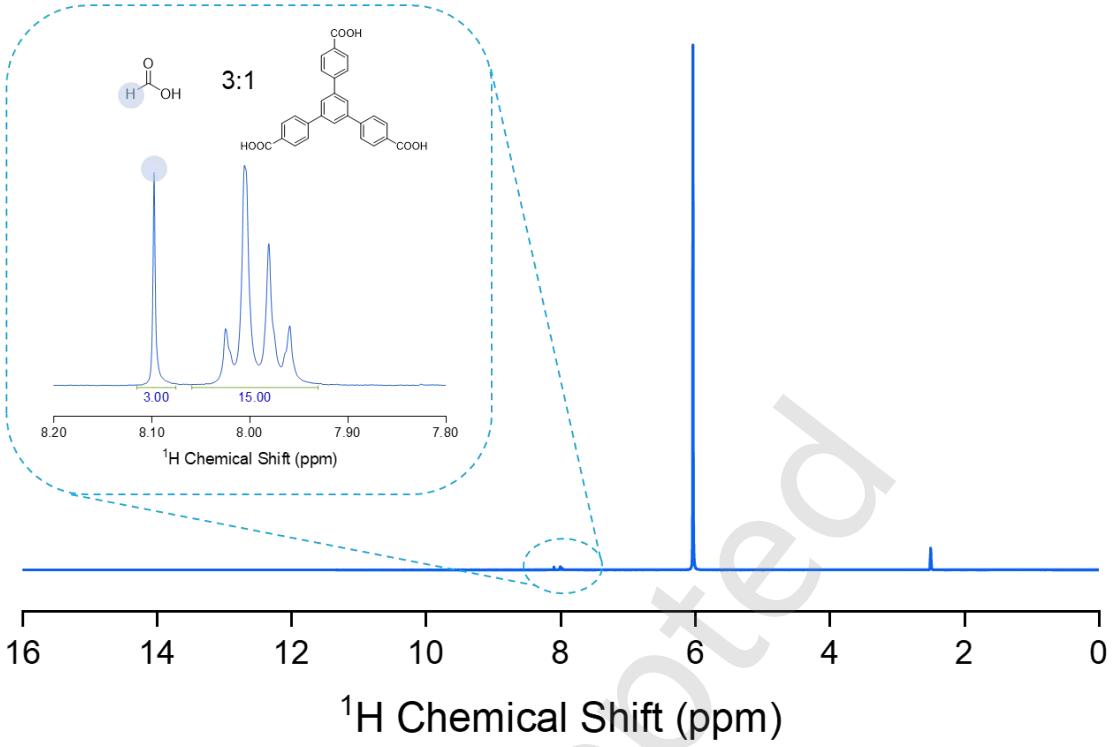

Figure S6. Digested-solution ^{1}H NMR spectrum of MOF-521 digested in DMSO-d_6 with DCl.

Just Accepted

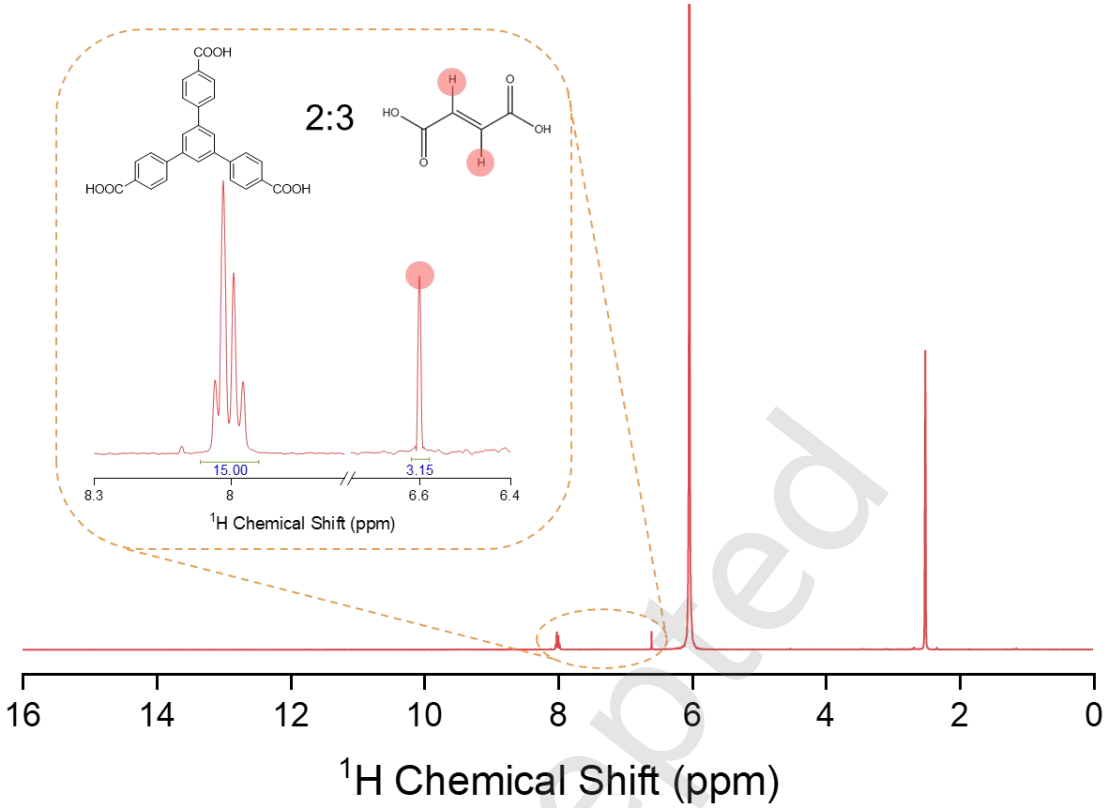

Figure S7. Digested-solution ^{1}H NMR spectrum of MOF-521-Fum digested in DMSO-d_6 with DCl.

Just Accepted

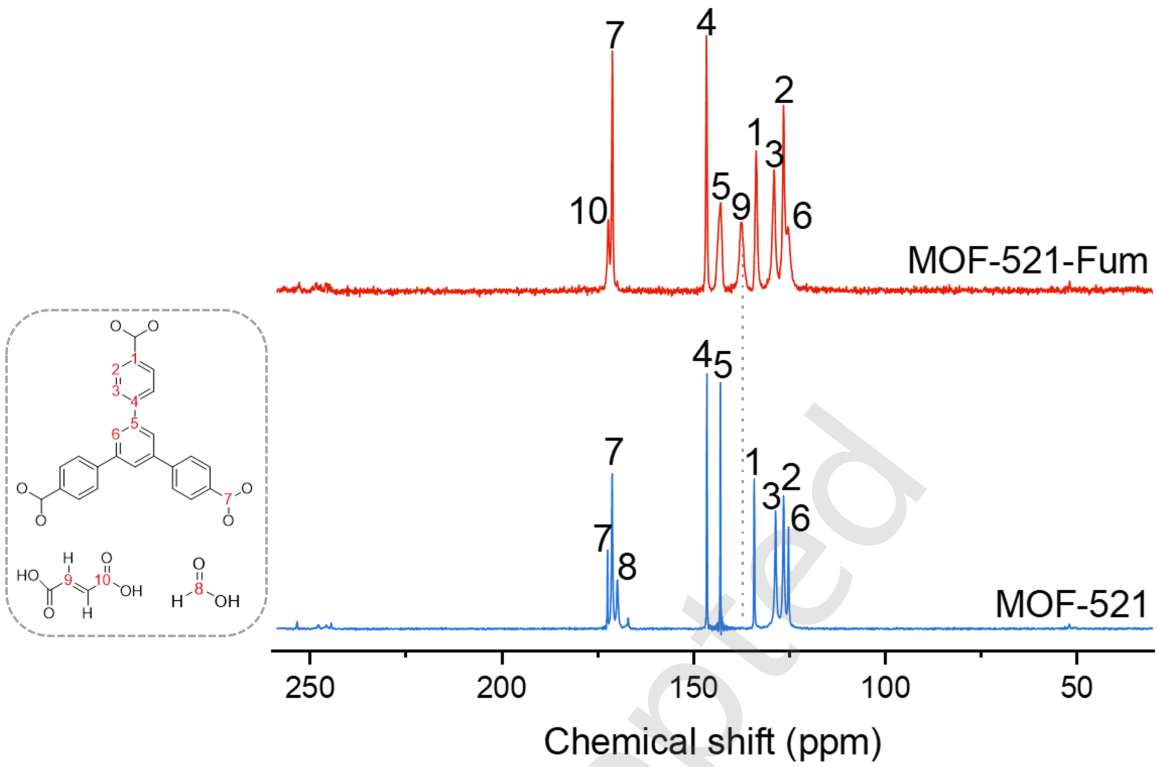

Figure S8. ^{13}C NMR spectrum of MOF-521-Fum.

Just Accepted

Table S3. 3D-ED information of MOF-521-Fum.

Name	MOF-521-Fum
Chemical formula	$C_{33}H_{20}O_{15}Al_3$
Temperature	298 K
Crystal system	Trigonal
Space group	*P3* (No.143)
Cell parameters	*a* = 39.97 Å, *c* = 6.49 Å 90° 90° 120°
Cell volume	8979 $Å^3$
Diffractometer	JEOL JEM-F200
Detector	ASI Cheetah 1800
Radiation	Electron (λ = 0.02508 Å under 200 KV)
Tilting range	-60.20° to 24.66°
Exposure time	0.500 S
Frame step	0.3611°
Frames	235
Data reduction	Pets2
Completeness	74.1% (to 1.49 Å)
Independent reflections	1655 (Rint = 0.1933)

Just Accepted

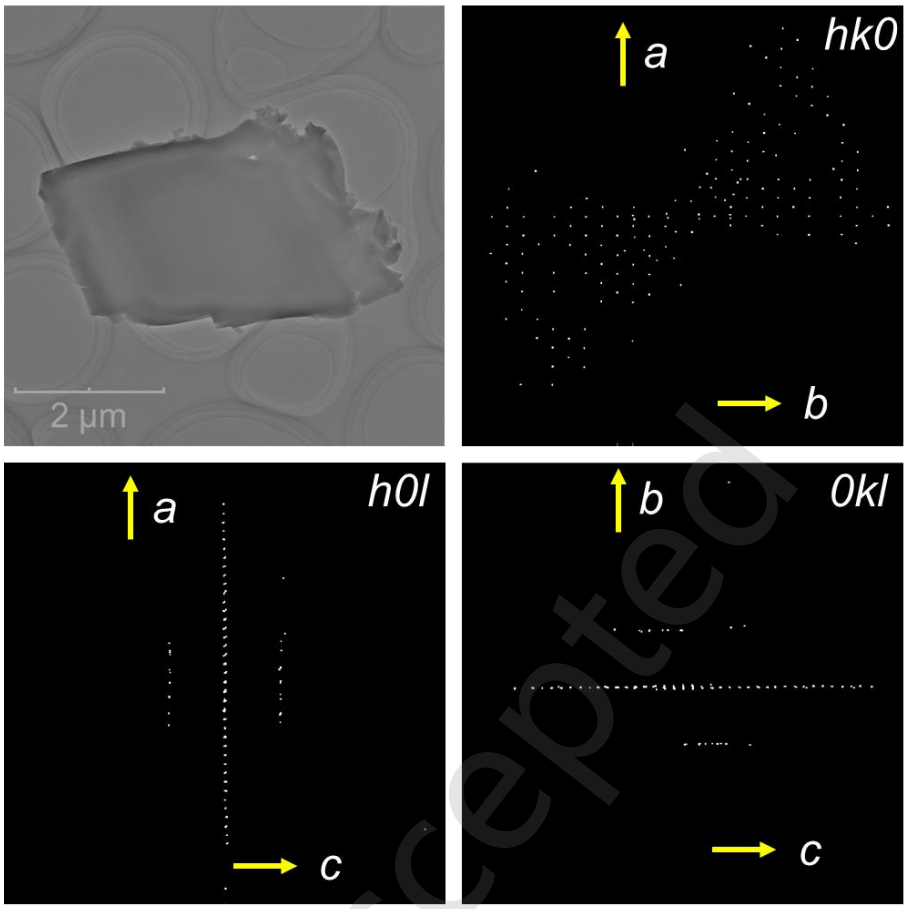

Figure S9. Reconstructed reciprocal lattice of 3D ED data of MOF-521-Fum. (a) SEM image, (b-d) 2D slices of 0kl, h0l, and hk0.

Just Accepted

Table S4 Rietveld Refined Cell Parameters for MOF-521-Fum.

Name	MOF-521-Fum
Moiety formula	$C_{33}H_{20}O_{15}Al_3$
Formula mass	737.45
Crystal system	Trigonal
Space group	*P*3 (**No**.143)
a (Å)	40.23
b (Å)	40.23
c (Å)	6.82
V (Å^3)	9554
Z	2
$d_{crystal}$ (g/cm^3)	0.769
R_p(%)	6.46%
R_{wp}(%)	9.88%
CCDC number	2576651

Just Accepted

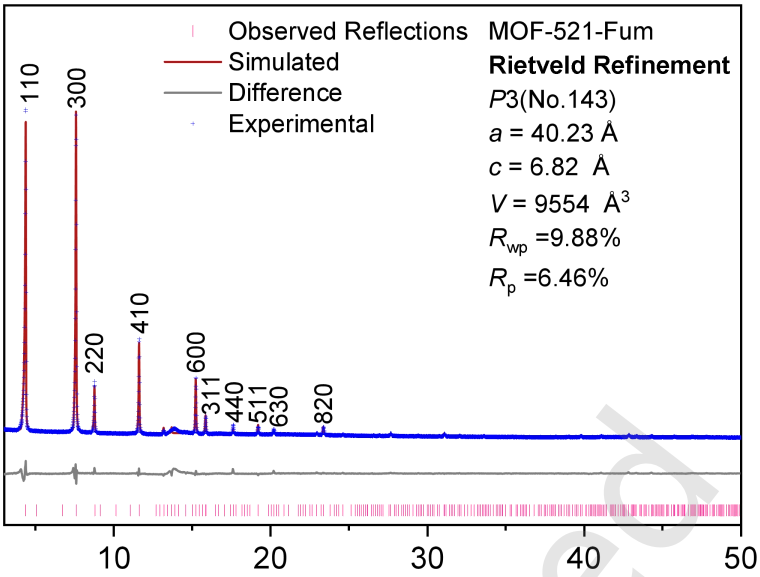

Figure S10. The comparison of experimental synchrotron PXRD patterns (blue) and refined profiles using the Rietveld method (red), along with their indexing, Bragg reflections (pink bar), and difference (grey) of MOF-521-Fum.

Just Accepted

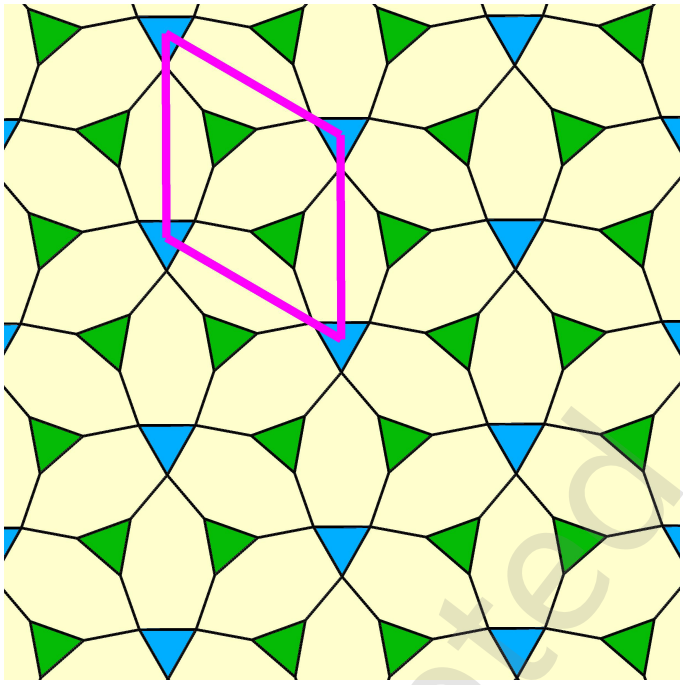

Figure S11. Simplified representation of the **cpe** net topology of the 2D structure, which constructs the MOF-521-Fum.

Just Accepted

Table S5. Proposed RCSR entry **wwq**.

Proposed **wwq**: transitivity [9 24]; new rod net with ladder + triangle; 2D projection **cpe**

name	space group	volume	density	td10
wwq	*P*312	11.085	110.878	770

a	*b*	*c*	*α*	*β*	*γ*
8.6567	8.6567	1.7085	90	90	120

vertices: 9

vertex	cn	x	y	z	symbolic	wyckoff	symmetry	order
V1	3	0.40954	0.36029	0.24959	x, y, z	6 l	1	1
V2	3	0.28458	0.25769	0.25179	x, y, z	6 l	1	1
V3	3	0.30698	0.38274	0.24866	x, y, z	6 l	1	1
V4	4	0.06119	0.06054	0.24882	x, y, z	6 l	1	1
V5	4	0.60665	0.33377	0.25078	x, y, z	6 l	1	1
V6	4	0.59981	0.13960	0.24997	x, y, z	6 l	1	1
V7	4	0.19460	0.12733	0.25023	x, y, z	6 l	1	1
V8	4	0.26639	0.47263	0.24992	x, y, z	6 l	1	1
V9	4	0.33285	0.60594	0.24912	x, y, z	6 l	1	1

edges: 24

edge	x	y	z	symbolic	wyckoff	symmetry	order
E1	0.56980	0.13960	0.50000	x, 2x-1, 1/2	3 k	2	2
E2	0.23632	0.47263	0.00000	x, 2x, 0	3 j	2	2
E3	0.34706	0.30899	0.25069	x, y, z	6 l	1	1
E4	0.56980	0.13960	0.00000	x, 2x-, 0	3 j	2	2

Just Accepted

E5	0.23632	0.47263	0.50000	x, 2x, 1/2	3 k	2	2
E6	0.63644	0.36356	0.50000	x, -x+1, 1/2	3 k	2	2
E7	0.29578	0.32022	0.25023	x, y, z	6 l	1	1
E8	0.47467	0.38024	0.24978	x, y, z	6 l	1	1
E9	0.35826	0.37152	0.24912	x, y, z	6 l	1	1
E10	0.23959	0.19251	0.25101	x, y, z	6 l	1	1
E11	0.36346	0.63654	0.00000	x, -x+1, 0	3 j	2	2
E12	0.63302	0.20624	0.25037	x, y, z	6 l	1	1
E13	0.12790	0.09393	0.24952	x, y, z	6 l	1	1
E14	0.19460	0.09730	0.50000	2x, x, 1/2	3 k	2	2
E15	0.06119	0.03059	0.00000	2x, x, 0	3 j	2	2
E16	0.30297	0.60594	0.00000	x, 2x, 0	3 j	2	2
E17	0.30297	0.60594	0.00000	x, 2x, 0	3 j	2	2
E18	0.60665	0.30333	0.50000	2x, x, 1/2	3 k	2	2
E19	0.29962	0.53928	0.24952	x, y, z	6 l	1	1
E20	0.30297	0.60594	0.50000	x, 2x, 1/2	3 k	2	2
E21	0.06119	0.03059	0.50000	2x, x, 1/2	3 k	2	2
E22	0.63644	0.36356	0.00000	x, -x+1, 0	3 j	2	2
E23	0.19460	0.09730	0.00000	2x, x, 0	3 j	2	2
E24	0.28669	0.42769	0.24929	x, y, z	6 l	1	1

Just Accepted

Section S4. Static Iodine Vapor Capture

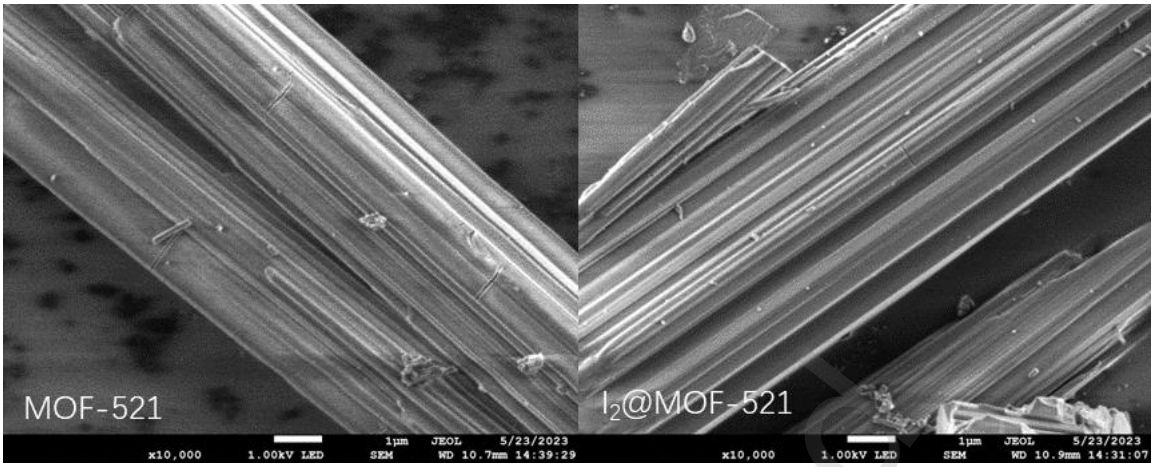

Figure S12. SEM images of MOF-521 before and after iodine loading.

Just Accepted

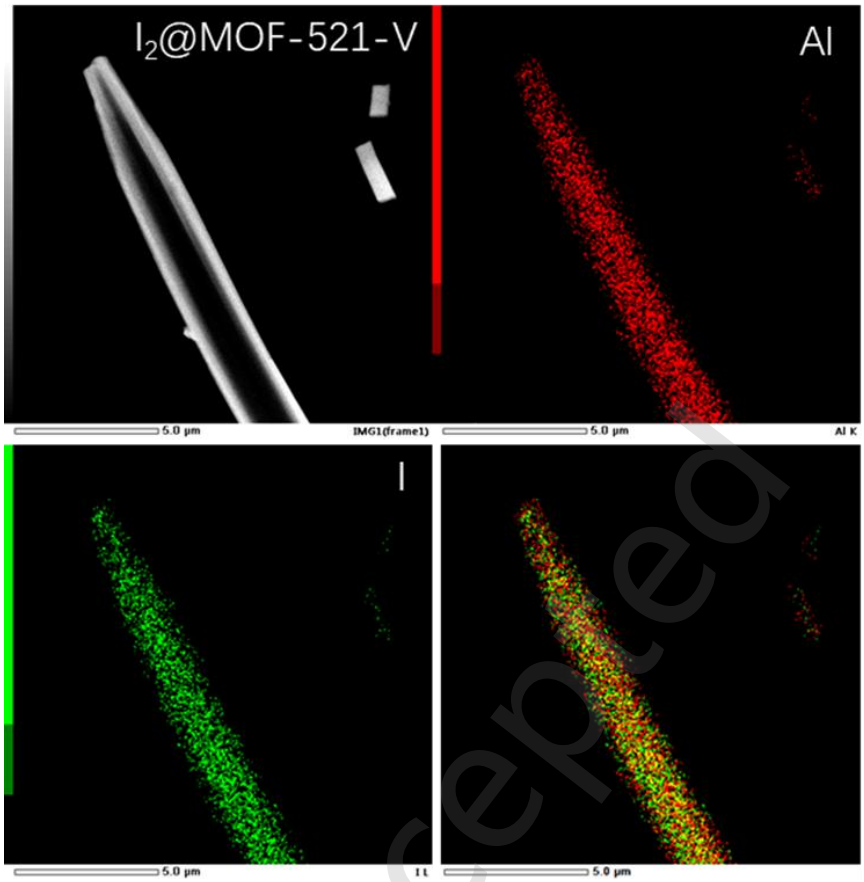

Figure S13 Element distribution and EDS spectra of MOF-521 after iodine loading.

Just Accepted

Table S6. Comparison of I_2 vapor uptake for pristine MOFs without additional functionalization. A criterion of iodine uptake exceeding 1.0 g g^{-1} was adopted to filtrate literatures, so as to concurrently evaluate both packing density and high iodine gravimetric capacity.

Materials	BET SA	V_p	crystal density	I_2 uptake	I_2 Packing density	I_2 volume adsorption capacity	Pore Space Utilization	Ref.
	$m^2\ g^{-1}$	$cm^3\ g^{-1}$	$g\ cm^{-3}$	$g\ g^{-1}$	$g\ cm^{-3}$	$cm^3\ cm^{-3}$	%	
MFM-300(Sc)	1250	0.5	1.02	1.54	3.08	0.32	62	1
ZIF-8	1630	0.66	0.88	1.25	1.89	0.22	38	2
UPC-158	2170	0.93	0.66	1.78	1.91	0.24	39	3
MOF-808	1930	0.82	0.86	2.18	2.66	0.38	54	4
NU-1000	2126	1.27	0.49	1.45	1.14	0.14	23	5
UiO-66	1170	0.43	1.18	1.17	2.72	0.28	55	6
PCN-333(Al)	2935	2.97	0.23	4.42	1.49	0.21	30	7
MIL-101	1738	0.87	0.44	2.67	3.07	0.24	62	8
HIAM-4014	2658	1.11	0.52	2.68	2.41	0.28	49	9
MBM	62	0.62	--	0.98	1.57	--	32	10
PCN-222	1893	1.1	0.49	2.61	2.37	0.26	48	11
$Zn_3(DL\text{-}lac)_2(pybz)_2$	763	0.4	1.08	1.00	2.48	0.22	51	12
$Zr_6O_4(OH)_4(sdc)_6$	2900	1.33	0.43	1.07	0.80	0.09	16	13
HKUST-1	1850	0.74	0.89	1.75	2.36	0.32	48	14
MOF-521	**1703**	**0.6**	0.85	**1.92**	**3.20**	0.33	**65**	**This work**
MOF-521-Fum	**1780**	**0.71**	0.77	**1.98**	**2.79**	0.31	**57**	**This work**
Solid Iodine density 4.93 $g\ cm^{-3}$								

Just Accepted

Data collection. The powder X-ray diffraction patterns (PXRD) of time-resolved, progressive I_2-loaded MOF-521 samples were collected on a Bruker D8 powder X-ray diffractometer using Cu *K*α (λ = 1.5418 Å) X-ray source.

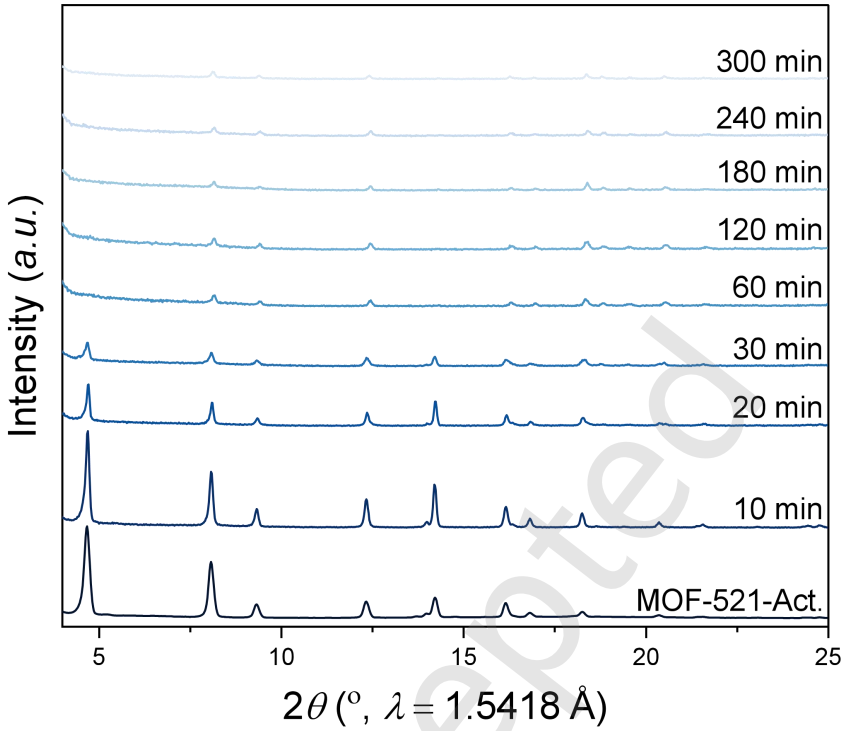

Figure S14. PXRD pattern of MOF-521 after different durations of iodine loading and desorption.

Just Accepted

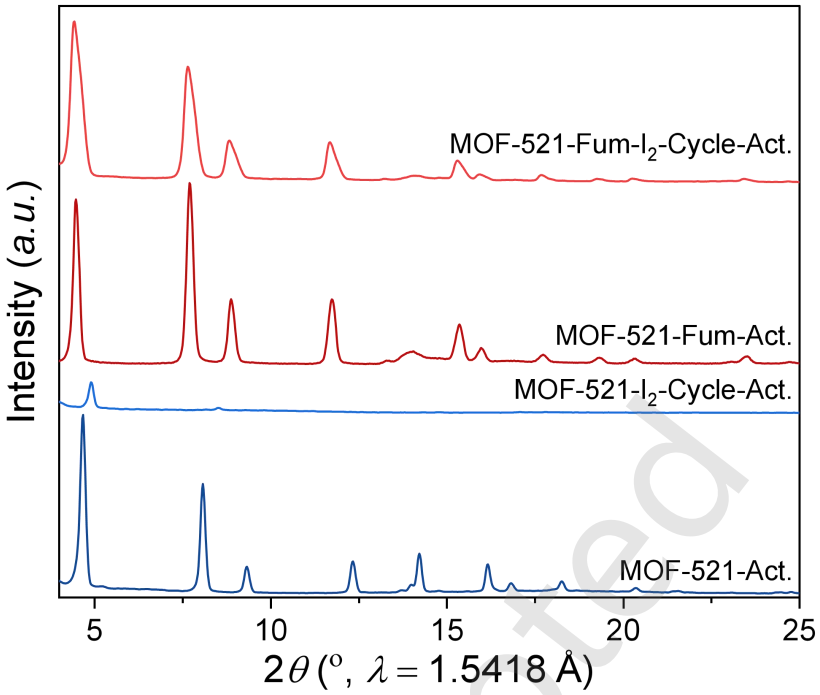

Figure S15. PXRD pattern of MOF-521 and MOF-521-Fum before and after 4th I_2 cycling tests.

Just Accepted

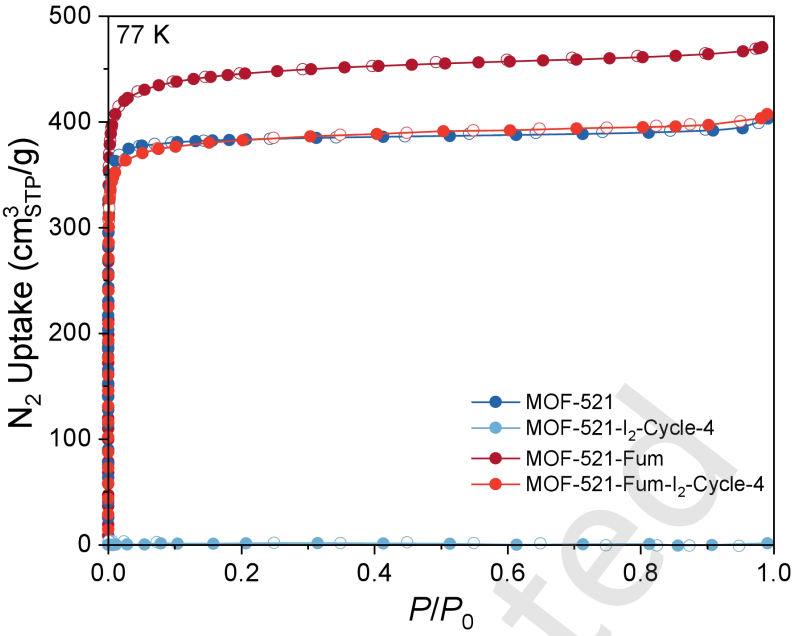

Figure S16. N_2 adsorption–desorption isotherms of MOF-521 and MOF-521-Fum before and after 4th I_2 cycling tests.

Just Accepted

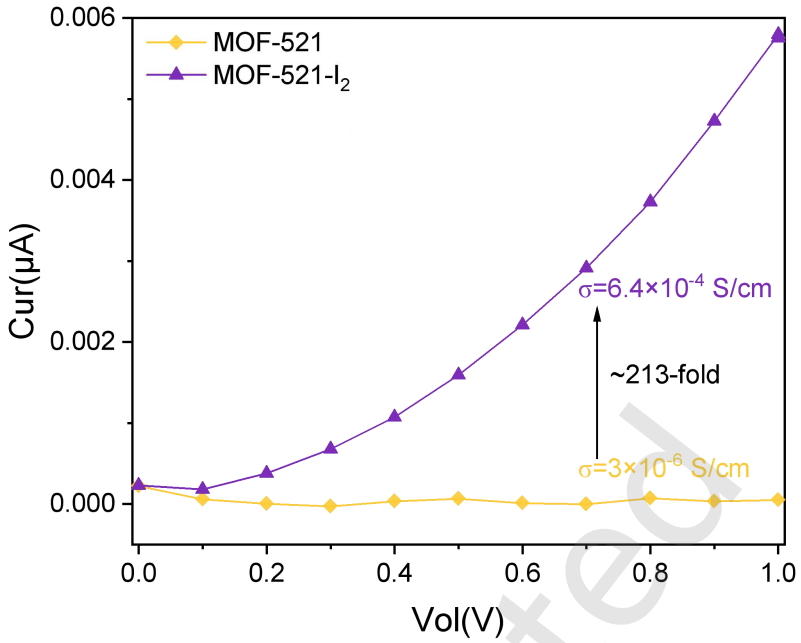

Figure S17 Electrical conductivity tests of MOF-521 before and after I_2 loading.

Just Accepted

Table S7. Comparative assessment on electrical conductivity.

Materials	Conductivity of bare MOF (S/cm)	Conductivity of iodine-loaded MOF (S/cm)	Ref.
$[Cu[Ni(pdt)_2]$	1×10^{-8}	1×10^{-4}	15
$[Cu_6(pybz)_8(OH)_2](I^-)_2$	8.04×10^{-9}	8.11×10^{-7}	16
$[Co_{1.5}(bdc)_{1.5}(H_2bpz)]$	2.59×10^{-9}	1.56×10^{-6}	17
$[Co(ebic)_2]_n$	2.46×10^{-9}	2.21×10^{-7}	18
$[Zn(ebic)_2]_n$	4.33×10^{-9}	3.47×10^{-7}	
$[Eu(L_1)]$	8.27×10^{-7}	2.71×10^{-5}	19
IFMC-15	2.59×10^{-9}	2.07×10^{-7}	20
$[(Me_2NH_2)_2]\cdot[Cd_3(5\text{-tbip})_4]_n$	1.71×10^{-8}	1.30×10^{-6}	21
MET-3	0.77×10^{-4}	1×10^{-3}	22
$[Tb_3(Cu_4I_4)_3(ina)_9]_n$	5.72×10^{-11}	2.16×10^{-4}	23
$[Zn_3(DL\text{-}lac)_2(pybz)_2]_n$	--	$\sigma^{\parallel} = 3.4\times10^{-3}$	13
	--	$\sigma^{\perp} = 1.7\times10^{-4}$	
$Mn(F_4TCNQ)(py)_2$	5×10^{-10}	1.4×10^{-4}	24
MFM-300(V)	1.7×10^{-10}	1.16×10^{-4}	25
SION-8	$< 10^{-9}$	5.3×10^{-6}	26
$Cu_3(HHTP)_2@I_2$	38	549	27
HKUST-1	1.00×10^{-7}	1.00×10^{-5}	28
$Co_3(NDC)_3DMF_4$	--	1.88×10^{-6}	29
$Cu_3(HHTN)_2$	9.55×10^{-10}	1×10^{-5}	30
$Cu_3(TABTO)_2$	1.00×10^{-9}	0.78	31
MOF-521	**3×10^{-6}**	**6.4×10^{-4}**	**This work**
solid iodine = 1×10^{-9} S/cm			

Just Accepted

Section S5. Dynamic Iodine Vapor Capture

The dynamic I_2 capture experiment was carried out using a home-made adsorption device, employing desolvated MOF-521 and MOF-521-Fum at the target temperature. In a typical experiment, 60.0 mg of the adsorbent was packed into a glass column (8.0 mm inner diameter, 1 mm wall thickness, 100 mm length), with silane-treated glass wool filling the void space. Iodine vapor was carried by an argon flow (6 mL min^{-1}) and controlled by a flowmeter, with the I_2 flow rate measured to be approximately 0.5 mg h^{-1}. A 0.1 M KI solution was used as the absorption solution to capture any I_2 molecules not adsorbed by MOF-521, converting them into I_3^-. A UV-vis spectrophotometer (l = 288 nm and 352 nm) was positioned facing the absorption solution, and spectra were collected every minute during the adsorption process. Meanwhile, a blank KI aqueous solution (0.1 M, 100 mL) was measured as a reference. In this way, the sample's time-dependent absorbance reflected the MOF's adsorption capacity. Finally, the I_2-loaded MOF-521 and MOF-521-Fum samples were characterized by TGA.

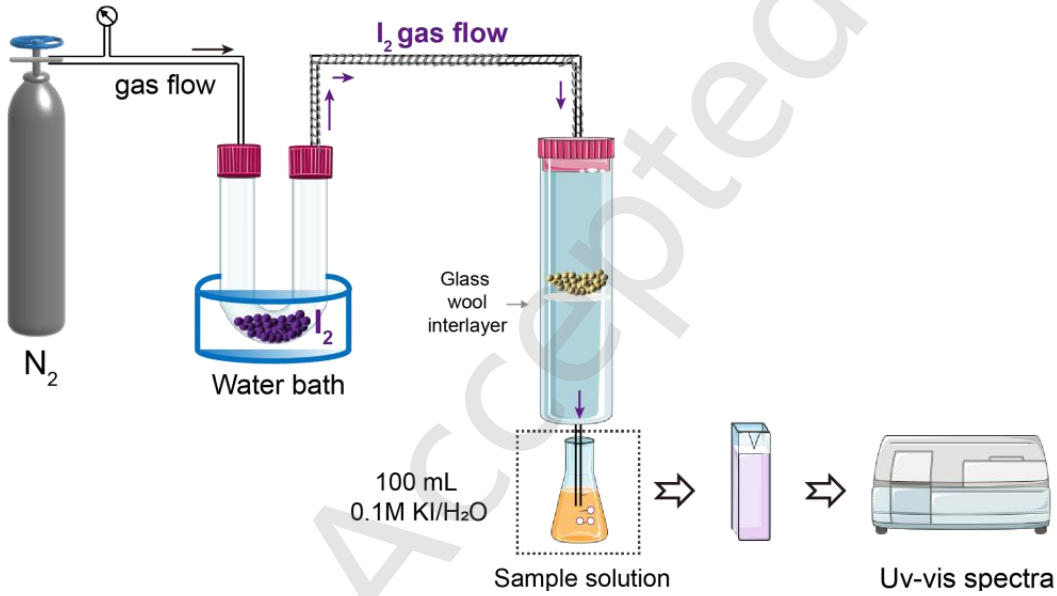

Figure S18. The schematic diagram of the device used to measure the iodine gas flow capture behavior of MOF-521 and MOF-521-Fum.

Just Accepted

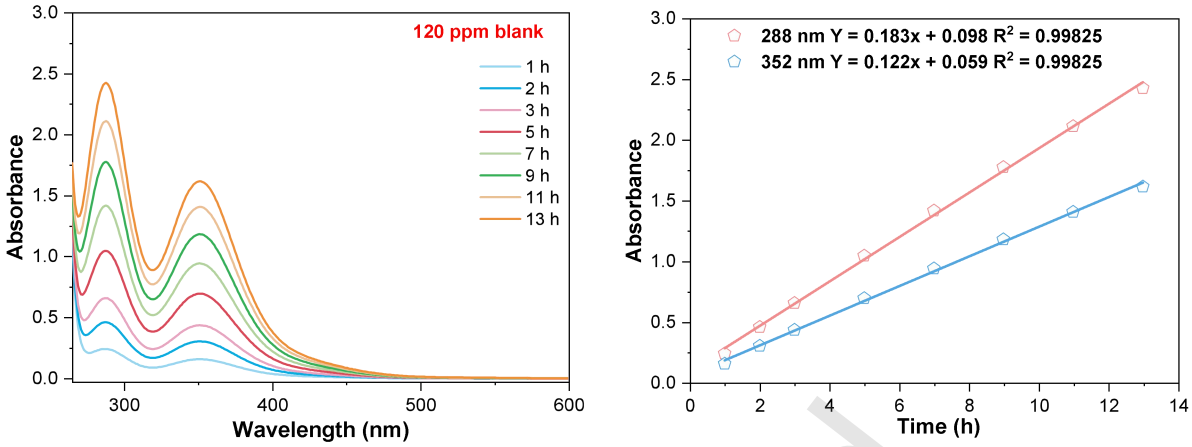

Figure S19. Time-dependent UV–vis spectra of the KI aqueous solution during exposure to a 120 ppm I_2/N_2 stream in the absence of adsorbent, with linear fitting of absorbance changes at 288 and 352 nm.

Just Accepted

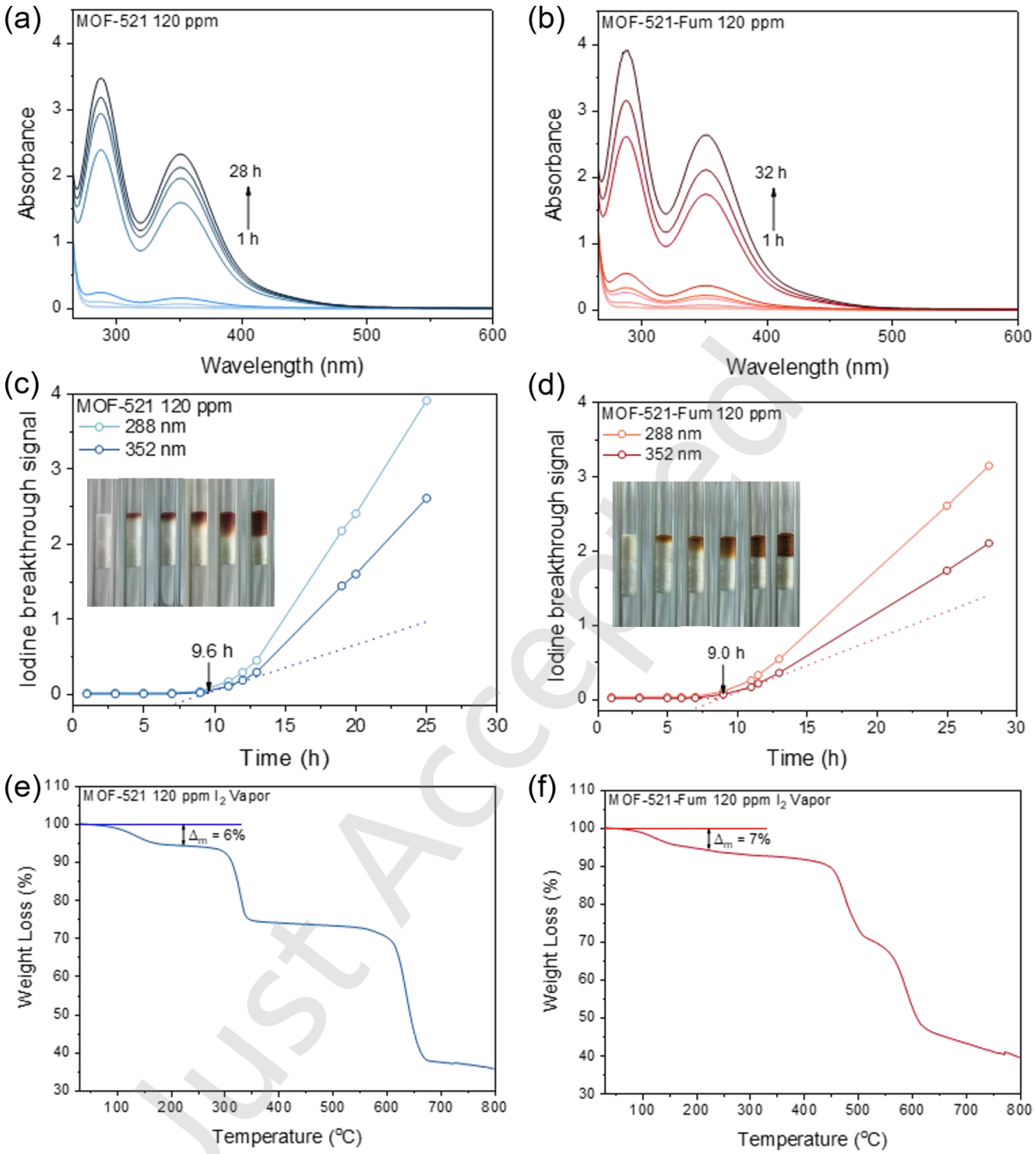

Figure S20. Dynamic iodine capture behavior of MOF-521 and MOF-521-Fum under a 120 ppm I_2/N_2 stream. (a,b) Time-dependent UV–vis spectra of iodine captured by KI solution during breakthrough experiments. (c,d) Corresponding iodine breakthrough curves with photographs of the outlet KI solutions. (e,f) TGA analysis of iodine-loaded MOF-521 and MOF-521-Fum.

Just Accepted

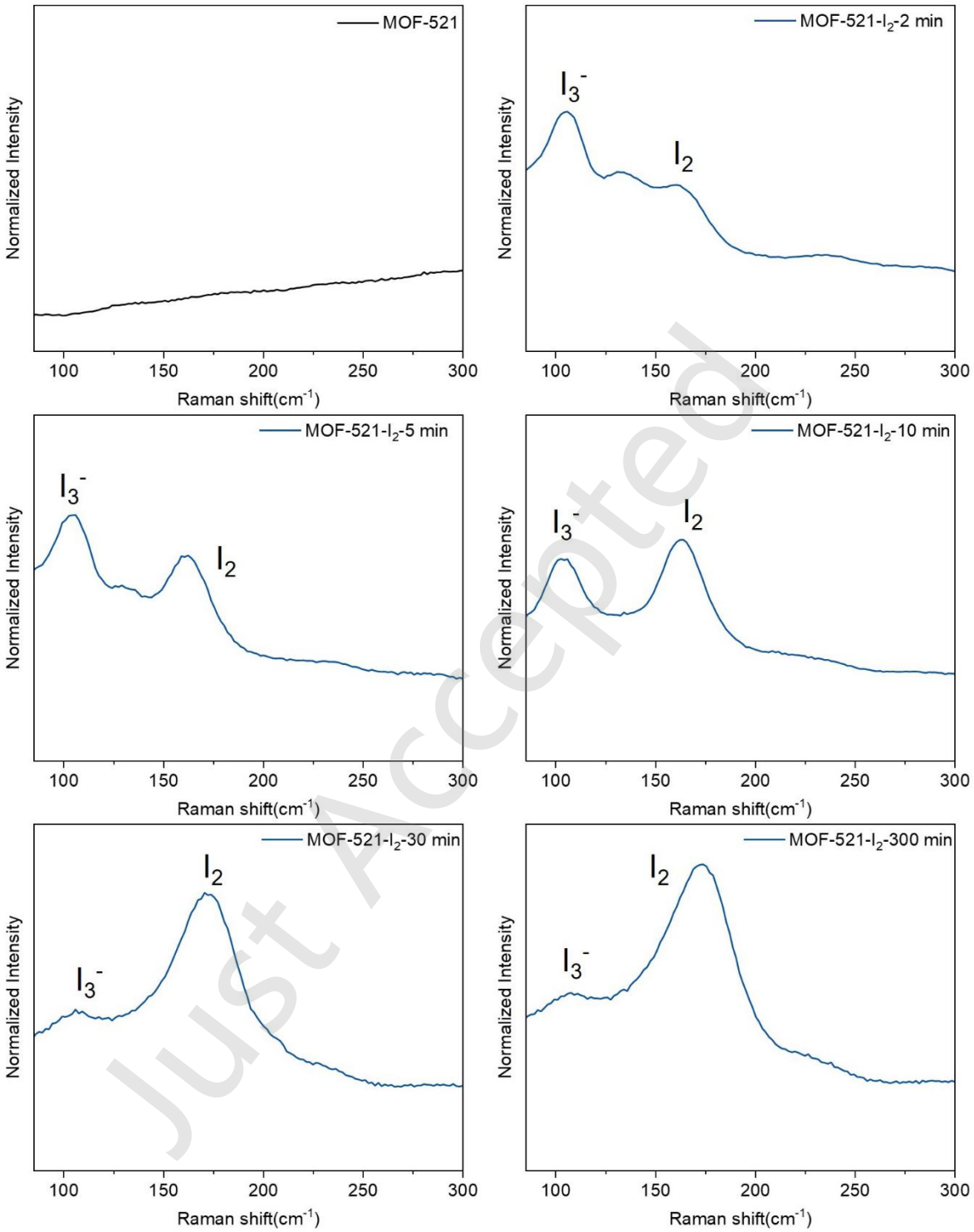

Figure S21. Raman spectrum of I_2-loaded MOF-521.

Just Accepted

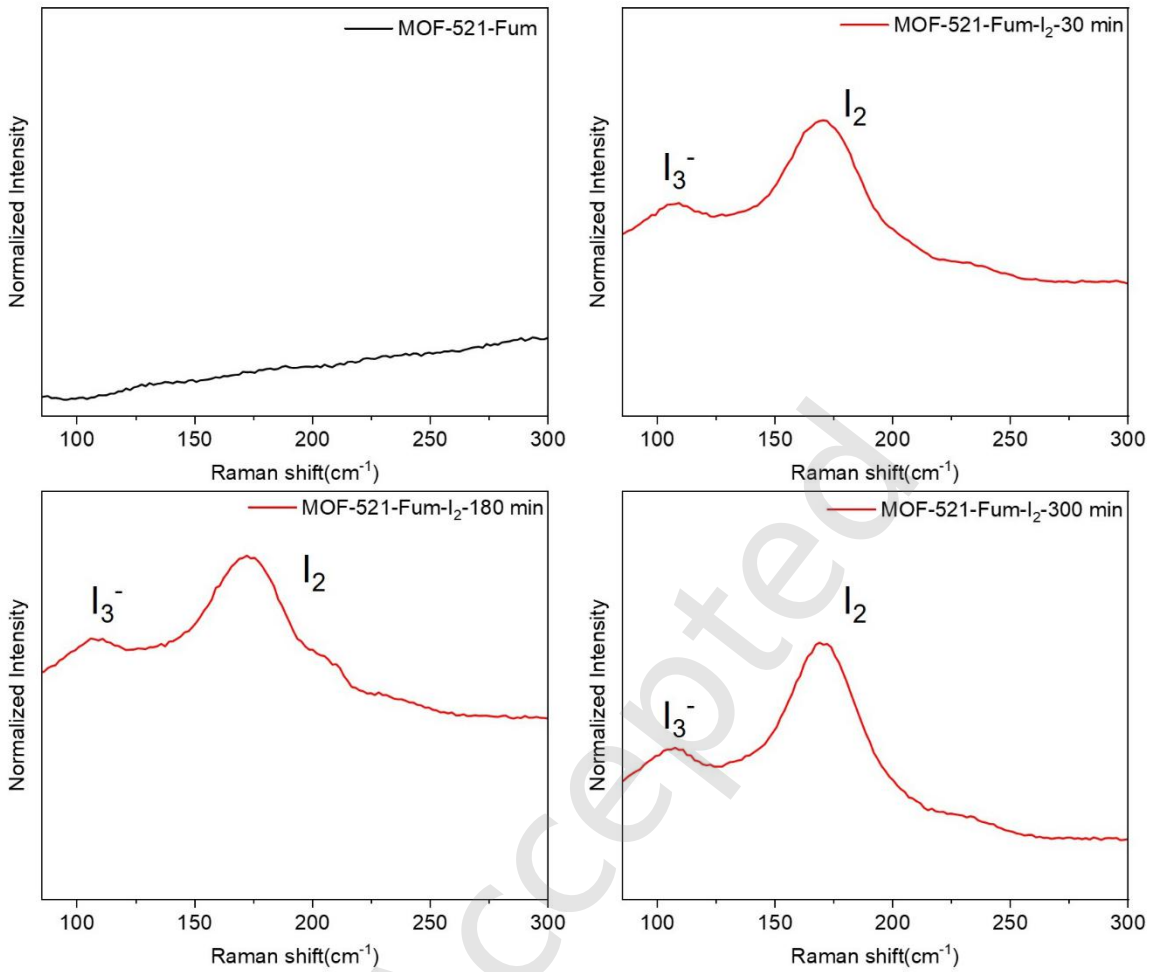

Figure S22. Raman spectrum of I_2-loaded MOF-521-Fum.

Just Accepted

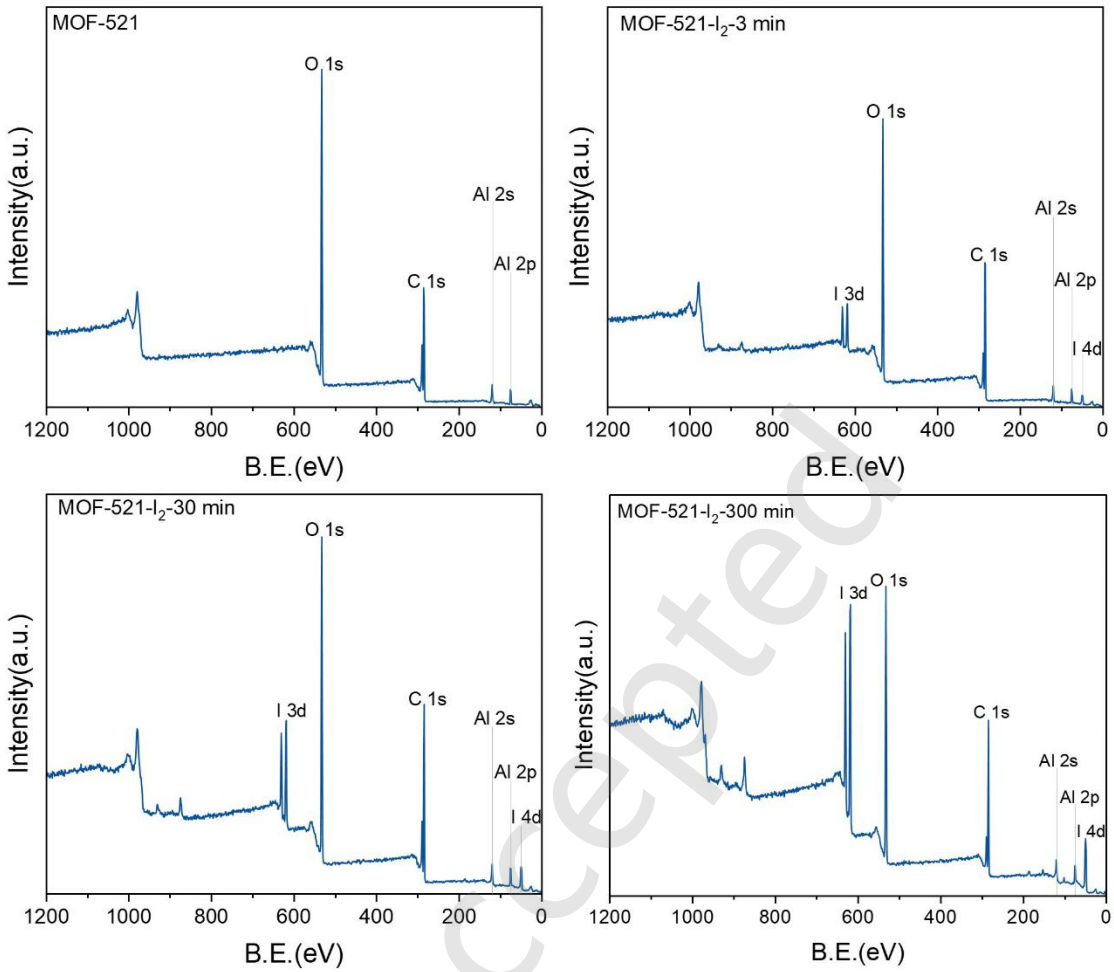

Figure S23. XPS spectra of I_2-loaded MOF-521.

Just Accepted

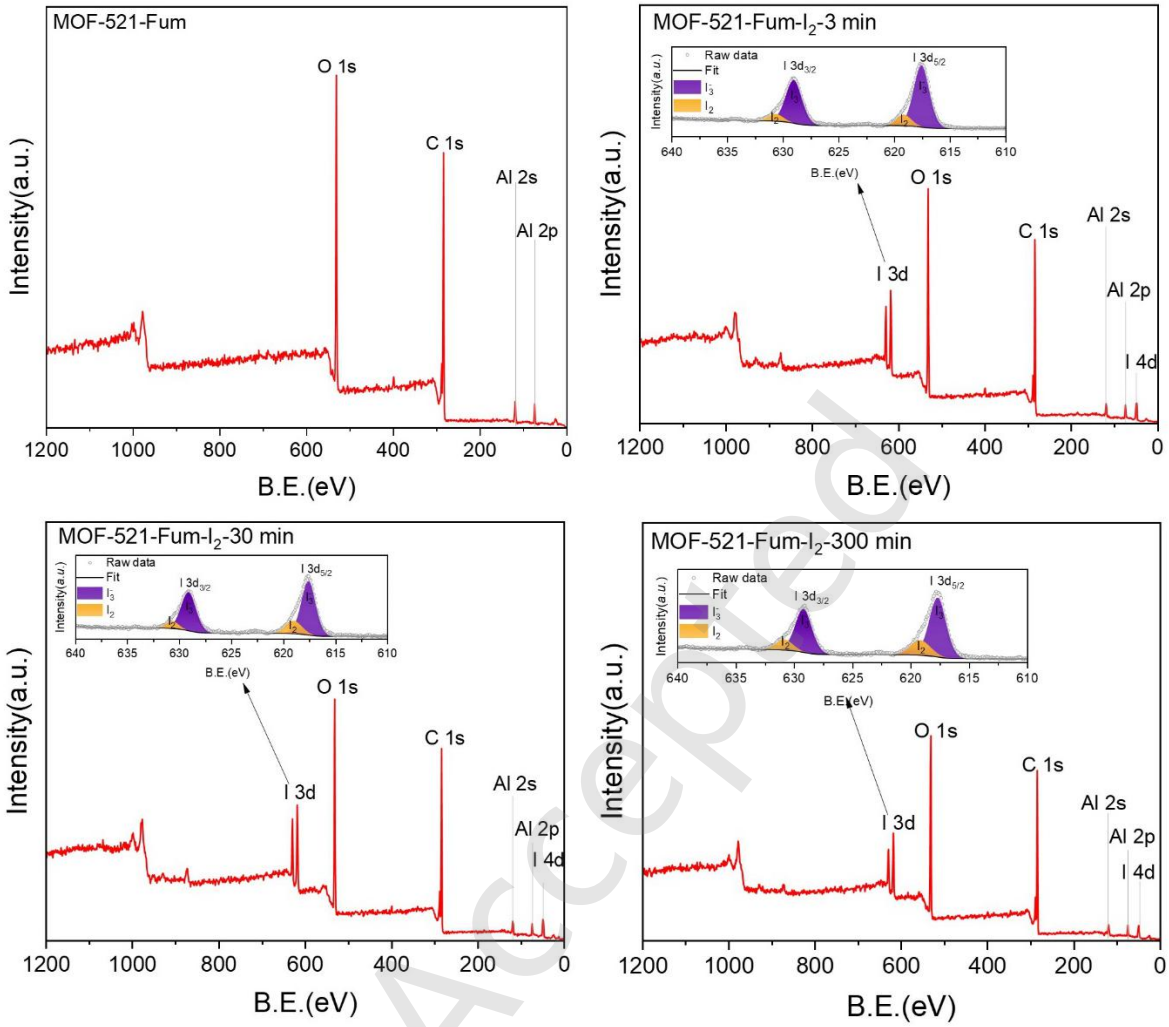

Figure S24. XPS spectra of I_2-loaded MOF-521-Fum.

Just Accepted

Section S6. Molecular Simulations and Interaction Analyses

Grand Canonical Monte Carlo (GCMC) simulations [32]. Grand canonical Monte Carlo (GCMC) simulations of I_2 adsorption isotherms at 298 K (0-1 bar) were implemented in the RASPA software package. The net atom charges (NACs) in the frameworks were computed using the density-derived electrostatic and chemical (DDEC) method. The Lennard-Jones (LJ)parameters of the metal atoms in the framework came from the universal force field(UFF), and those of the nonmetal elements came from the DREIDING force field. Total number of simulation cycles was set as 200,000, with 100,000 cycles forinitialization and 100,000 cycles for production, to reach the convergence, and thevalues were obtained by taking the average.

Density Functional Theory (DFT) calculation. All structures obtained experimentally via SCXRD were optimized using DFT calculations with the CP2K software to compute energies and forces and refine hydrogen positions.

For Kohn-Sham Density Functional Theory energy and force calculations, we used the DZVP-MOLOPT-SR-GTH basis set and the GTH-PBE pseudopotential. Atoms were constrained during the evaluation of forces using the QUICKSTEP method, which utilizes the Density Functional Theory with Gaussian and Planewaves (GPW) method. The exchange correlation density functional we use is PBE, along with the D3(BJ) dispersion correction, which is consistent with the basis set and pseudopotential we have chosen.

Geometry optimization calculations are performed to find the local minima, and the cell dimensions are chosen to be fixed. The parameters for the section of energy and force calculation are the same as above. The algorithm for finding the stationary points is the BFGS method. When refining the positions of hydrogen atoms, the movements of all other atoms are constrained.

Independent Gradient Model based on Hirshfeld partition of molecular density (IGMH) Analyses. The independent gradient model based on the Hirshfeld partition of molecular density (IGMH) method, reported by Lu et al. in 2022, was used to explore the linker-linker interactions. The IGMH method is an improved version of the independent gradient mode (IGM), which replaces the free-state atomic densities used in IGM with atomic densities derived from the Hirshfeld partition of the actual molecular electron density.

The dg function are defined as the difference between IGM type of density gradient (g^{IGM}) and the gradient of promolecular density (g). This parameter has a positive correlation with the strength of intermolecular interactions within an interatomic interaction region and can thus be used to measure the relative strength of these interactions.

The intermolecular interactions can be expressed as:

$$dg^{inter}(r) = g^{IGM,inter}(r) - g^{inter}(r)$$

with

$$g^{inter}(r) = \left| \sum_{A} \sum_{i \epsilon A} \nabla \rho_i^{free}(r) \right|$$

where r represents the Cartesian coordinate vector, A loops over all fragments, i loops all atoms in the corresponding fragment and ρ_i^{free} represents the spherically averaged density of atom i in its free state.

For quantitative analyses of host-guest interactions, the independent gradient model based on Hirshfeld partitioning of molecular density (IGMH) was applied to the periodic crystal structures of MOF phases using Multiwfn. For these MOFs with periodic structures, CP2K software was used to generate the wave functions by DFT calculations using the PBE-D3(BJ) exchange–correlation functional at the DZVP-MOLOPT-SR-GTH level.

Intercepting guests and MOF-521 for host-guest IGMH calculations, we focus only on the intermolecular interactions, denoted as dg-inter. and decompose the inter-framework interactions into the contributions of each atom, denoted as the dg-index; the larger the dg-index, the greater the atom's contribution to the interactions. And use VMD to color the atoms by

Just Accepted

dg-index to show in the structure.

Just Accepted

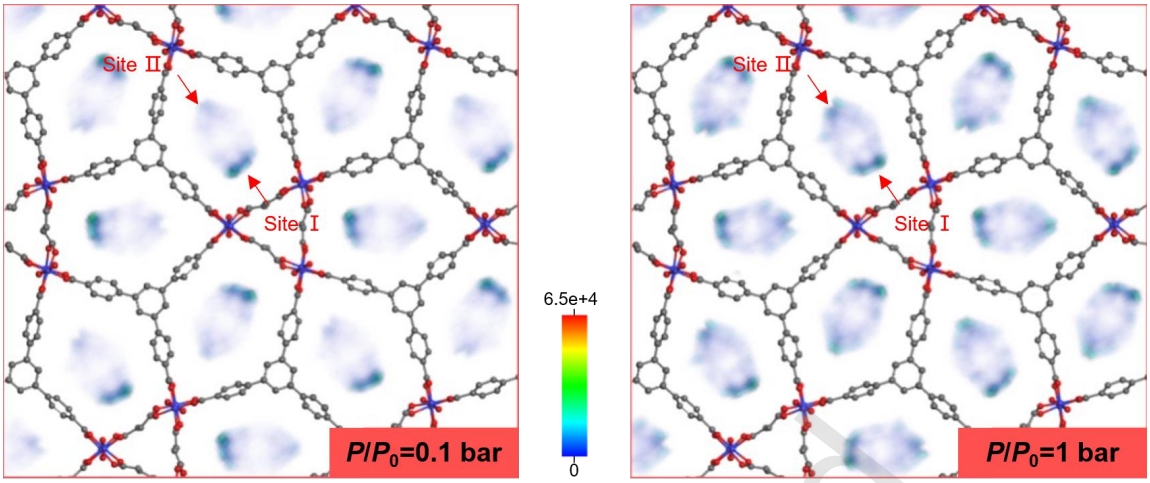

Figure S25. GCMC simulation of MOF-521-Fum at different chemical potentials revealed the probability of iodine adsorption. It showed that site I was filled first, followed by site II.

Just Accepted

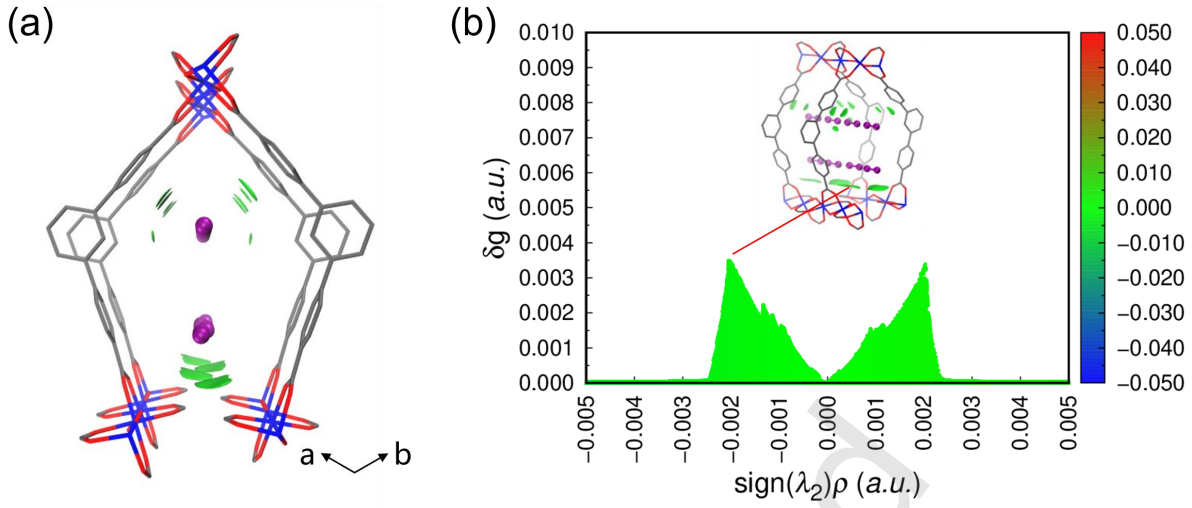

Figure S26. (a) IGMH isosurface visualization of I_2–framework interactions in MOF-521, showing the spatial distribution of noncovalent interactions between confined iodine molecules and the pore walls. (b) Corresponding IGMH scatter plot revealing the predominance of weak attractive dispersion interactions between I_2–framework.

Just Accepted

References

[1] Zhang, X.; da Silva, I.; Godfrey, H. G. W.; Callear, S. K.; Sapchenko, S. A.; Cheng, Y.; Vitorica-Yrezabal, I.; Frogley, M. D.; Cinque, G.; Tang, C. C. Confinement of Iodine Molecules into Triple-Helical Chains within Robust Metal-Organic Frameworks. *J. Am. Chem. Soc.* **2017**, 139 (45), 16289-16296.

[2] Sava, D. F.; Rodriguez, M. A.; Chapman, K. W.; Chupas, P. J.; Greathouse, J. A.; Crozier, P. S.; Nenoff, T. M. Capture of volatile iodine, a gaseous fission product, by zeolitic imidazolate framework-8. *J. Am. Chem. Soc.* **2011**, 133 (32), 12398-12401.

[3] Guo, B.; Li, F.; Wang, C.; Zhang, L.; Sun, D. A rare (3,12)-connected zirconium metal–organic framework with efficient iodine adsorption capacity and pH sensing. *J. Mater. Chem. A.* **2019**, 7 (21), 13173-13179.

[4] Wang, L.; Chen, P.; Dong, X.; Zhang, W.; Zhao, S.; Xiao, S.; Ouyang, Y. Porous MOF-808@PVDF beads for removal of iodine from gas streams. *RSC Adv.* **2020**, 10 (73), 44679-44687.

[5] Hanna, S. L.; Rademacher, D. X.; Hanson, D. J.; Islamoglu, T.; Olszewski, A. K.; Nenoff, T. M.; Farha, O. K. Structural Features of Zirconium-Based Metal–Organic Frameworks Affecting Radiolytic Stability. *Ind. Eng. Chem. Res.* **2020**, 59 (16), 7520-7526.

[6] Maddock, J.; Kang, X.; Liu, L.; Han, B.; Yang, S.; Schröder, M. The Impact of Structural Defects on Iodine Adsorption in UiO-66. *Chemistry.* **2021**, 3 (2), 525-531.

[7] Tang, Y.; Huang, H.; Li, J.; Xue, W.; Zhong, C. IL-induced formation of dynamic complex iodide anions in IL@MOF composites for efficient iodine capture. *J. Mater. Chem. A.* **2019**, 7 (31), 18324-18329.

[8] Tang, P.; Xie, X.-X.; Huang, Z.-Y.; Cai, X.-T.; Zhang, W.-G.; Cai, S.-L.; Fan, J.; Zheng, S.-R. Ethylenediamine grafted MIL-101 for iodine vapor capture with high capacity. *J. Solid State Chem.* **2022**, 315.

[9] Xia, H. L.; Zhou, K.; Yu, L.; Wang, H.; Liu, X. Y.; Li, J. A Zirconium-Organic Framework Constructed from Saddle-Shaped Tetratopic Carboxylate for High-Rate and -Efficiency Iodine Capture. *Inorg. Chem.* **2022**, 61 (43), 17109-17114.

[10] He, T.; Xu, X.; Ni, B.; Lin, H.; Li, C.; Hu, W.; Wang, X. Metal–Organic Framework Based Microcapsules. *Angew. Chem. Int. Ed.* **2018**, 57 (32), 10148-10152.

[11] Zhang, J.; Wang, X.; Guo, X.; Sang, W.; He, Q.; Zhang, W. Crystal- and Pore-Size Dependent Iodine Adsorption Properties in MOFs. *Small.* **2025**, 21 (13), 2410678.

[12] Zeng, M.-H.; Wang, Q.-X.; Tan, Y.-X.; Hu, S.; Zhao, H.-X.; Long, L.-S.; Kurmoo, M. Rigid Pillars and Double Walls in a Porous Metal-Organic Framework: Single-Crystal to Single-Crystal, Controlled Uptake and Release of Iodine and Electrical Conductivity. *J. Am. Chem. Soc.* **2010**, 132 (8), 2561-2563.

[13] Marshall, R. J.; Griffin, S. L.; Wilson, C.; Forgan, R. S. Stereoselective Halogenation of Integral Unsaturated C-C Bonds in Chemically and Mechanically Robust Zr and Hf MOFs. *Chem. Eur. J.* **2016**, 22 (14), 4870-4877.

[14] Sava, D. F.; Chapman, K. W.; Rodriguez, M. A.; Greathouse, J. A.; Crozier, P. S.; Zhao, H.; Chupas, P. J.; Nenoff, T. M. Competitive I_2 Sorption by Cu-BTC from Humid Gas Streams. *Chemistry of Materials.* **2013**, 25 (13), 2591-2596. DOI: 10.1021/cm401762g.

[15] Kobayashi, Y.; Jacobs, B.; Allendorf, M. D.; Long, J. R. Conductivity, Doping, and Redox Chemistry of a Microporous Dithiolene-Based Metal–Organic Framework. *Chem. Mater.* **2010**, 22 (14), 4120-4122.

[16] Yin, Z.; Wang, Q.-X.; Zeng, M.-H. Iodine Release and Recovery, Influence of Polyiodide Anions on Electrical Conductivity and Nonlinear Optical Activity in an Interdigitated and Interpenetrated Bipillared-Bilayer Metal–Organic Framework. *J. Am. Chem. Soc.* **2012**, 134 (10), 4857-4863.

[17] Li, G.-P.; Zhang, K.; Zhao, H.-Y.; Hou, L.; Wang, Y.-Y. Increased Electric Conductivity upon I_2 Uptake and Gas Sorption in a Pillar-Layered Metal–Organic Framework. *ChemPlusChem.* **2017**, 82 (5), 716-720.

[18] Yu, F.; Li, D.-D.; Cheng, L.; Yin, Z.; Zeng, M.-H.; Kurmoo, M. Porous Supramolecular Networks Constructed of One-Dimensional Metal–Organic Chains: Carbon Dioxide and Iodine Capture. *Inorg. Chem.* **2015**, 54 (4), 1655-1660.

Just Accepted

[19] Hao, Z.; Yang, G.; Song, X.; Zhu, M.; Meng, X.; Zhao, S.; Song, S.; Zhang, H. A europium(iii) based metal–organic framework: bifunctional properties related to sensing and electronic conductivity. *J. Mater. Chem. A*. **2014**, 2 (1), 237-244.

[20] He, W.-W.; Li, S.-L.; Yang, G.-S.; Lan, Y.-Q.; Su, Z.-M.; Fu, Q. Controllable synthesis of a non-interpenetrating microporous metal–organic framework based on octahedral cage-like building units for highly efficient reversible adsorption of iodine. *Chem. Commun.* **2012**, 48 (80), 10001-10003.

[21] Chaudhari, A. K.; Mukherjee, S.; Nagarkar, S. S.; Joarder, B.; Ghosh, S. K. Bi-porous metal–organic framework with hydrophilic and hydrophobic channels: selective gas sorption and reversible iodine uptake studies. *CrystEngComm.* **2013**, 15 (45), 9465-9471.

[22] Gándara, F.; Uribe-Romo, F. J.; Britt, D. K.; Furukawa, H.; Lei, L.; Cheng, R.; Duan, X.; O'Keeffe, M.; Yaghi, O. M. Porous, Conductive Metal-Triazolates and Their Structural Elucidation by the Charge-Flipping Method. *Chem. Eur. J.* **2012**, 18 (34), 10595-10601.

[23] Hu, Y.-Q.; Li, M.-Q.; Wang, Y.; Zhang, T.; Liao, P.-Q.; Zheng, Z.; Chen, X.-M.; Zheng, Y.-Z. Direct Observation of Confined $I^-\cdots I_2\cdots I^-$ Interactions in a Metal–Organic Framework: Iodine Capture and Sensing. *Chem. Eur. J.* **2017**, 23 (35), 8409-8413.

[24] Elliott, R. W.; Sutton, A. L.; Abrahams, B. F.; D'Alessandro, D. M.; Goerigk, L.; Hua, C.; Hudson, T. A.; Robson, R.; White, K. F. Multifunctional Coordination Polymer Exhibiting Reversible Mechanical Motion Allowing Selective Uptake of Guests and Leading to Enhanced Electrical Conductivity. *Inorg. Chem.* **2021**, 60 (17), 13658-13668.

[25] Zhang, X.; da Silva, I.; Fazzi, R.; Sheveleva, A. M.; Han, X.; Spencer, B. F.; Sapchenko, S. A.; Tuna, F.; McInnes, E. J. L.; Li, M.; et al. Iodine Adsorption in a Redox-Active Metal-Organic Framework: Electrical Conductivity Induced by Host-Guest Charge-Transfer. *Inorg. Chem.* **2019**, 58 (20), 14145-14150.

[26] Gładysiak, A.; Nguyen, T. N.; Spodaryk, M.; Lee, J.-H.; Neaton, J. B.; Züttel, A.; Stylianou, K. C. Incarceration of Iodine in a Pyrene-Based Metal–Organic Framework. *Chem. Eur. J.* **2019**, 25 (2), 501-506. DOI: https://doi.org/10.1002/chem.201805073.

[27] Gonzalez-Juarez, M. d. L.; Isaacs, M. A.; Bradshaw, D.; Nandhakumar, I. Enhanced Thermoelectric Properties of a Semiconducting Two-Dimensional Metal–Organic Framework via Iodine Loading. *ACS Appl. Mater. Interfaces.* **2023**, 15 (4), 5478-5486. DOI: 10.1021/acsami.2c20770.

[28] Gascon, J.; Aguado, S.; Kapteijn, F. Manufacture of dense coatings of $Cu_{3(}BTC)_2$ (HKUST-1) on α-alumina. *Micropor. Mesopor. Mater.* **2008**, 113 (1), 132-138. DOI: https://doi.org/10.1016/j.micromeso.2007.11.014.

[29] Lee, D. Y.; Kim, E.-K.; Shrestha, N. K.; Boukhvalov, D. W.; Lee, J. K.; Han, S.-H. Charge Transfer-Induced Molecular Hole Doping into Thin Film of Metal–Organic Frameworks. *ACS Appl. Mater. Interfaces.* **2015**, 7 (33), 18501-18507. DOI: 10.1021/acsami.5b04771.

[30] Meng, Z.; Mirica, K. A. Two-dimensional d-π conjugated metal-organic framework based on hexahydroxytrinaphthylene. *Nano Research.* **2021**, 14 (2), 369-375. DOI: 10.1007/s12274-020-2874-x.

[31] Jiang, Y.; Oh, I.; Joo, S. H.; Seo, Y.-S.; Lee, S. H.; Seong, W. K.; Kim, Y. J.; Hwang, J.; Kwak, S. K.; Yoo, J.-W.; et al. Synthesis of a Copper 1,3,5-Triamino-2,4,6-benzenetriol Metal–Organic Framework. *J. Am. Chem. Soc.* **2020**, 142 (43), 18346-18354. DOI: 10.1021/jacs.0c02389.

[32] Campañá, C.; Mussard, B.; Woo, T. K. Electrostatic Potential Derived Atomic Charges for Periodic Systems Using a Modified Error Functional. *J. Chem. Theory Comput.* **2009**, 5 (10), 2866-2878. DOI: 10.1021/ct9003405.

Just Accepted